

**EVALUATION OF MORPHOLOGY DESCRIPTORS
IN CT IMAGES OF THE AORTA
AS INDICATORS OF THE PRESENCE OF PLAQUE**

Susan L. Gordon

Submitted to the faculty of the University Graduate School
in partial fulfillment of the requirements
for the degree

Master of Science in Applied Mathematics and Computer Science

in the Department of Computer Science,
Indiana University
November 2009

Accepted by the Graduate Faculty, Indiana University, in partial fulfillment of the requirements for the degree of Master of Science.

James Wolfer, Ph.D.

Dana Vrajitoru, Ph.D.

Morteza Shafii-Mousavi, Ph.D.

Jeffrey Soble, M.D.

ACKNOWLEDGMENTS

In completing this graduate thesis, I am grateful for the support and encouragement that many people have provided to me.

I would like to thank Dr. James Wolfer for teaching, advising, and encouraging me throughout this journey. I would also like to thank my thesis committee members, Dr. Dana Vrajitoru and Dr. Morteza Shafii-Mousavi for their careful reading and suggestions for improvement.

Special thanks are extended to Dr. Jeffery Soble from Rush University Medical Center in Chicago, Illinois for serving on my thesis committee. I am grateful for all of the time that he spent helping to define this project, providing the CT datasets, and reviewing the thesis document. Dr. Soble and his colleagues, Dr. Ameet Parikh and Dr. David Chawla, also served as our domain experts in classifying the images. This project could not have been completed without their medical expertise.

Thank you to Dr. Robert Batzinger, Informatics Lab Supervisor, for arranging lab access and for his help in installing required software to complete the project.

The Computer Science Department at IU South Bend has a unique group of faculty and staff members who have been exceptionally positive and willing to help me succeed in this graduate program. I have enjoyed meeting, working with, and learning from them.

Last, I extend my love and special thanks to my husband and children who believed that I could do this.

Table of Contents

ACKNOWLEDGMENTS	iii
List of Illustrations	vi
ABSTRACT	1
1. INTRODUCTION	2
1.1 Cardiovascular System.....	2
1.2 Atherosclerosis.....	4
1.3 Computed Tomography	6
2. LITERATURE REVIEW	10
2.1 Image Segmentation.....	10
2.2 Image Descriptors	11
3. METHODOLOGY	12
3.1 Overview.....	12
3.2 Datasets	13
3.3 Software Summary.....	14
3.4 Selection.....	14
3.5 Segmentation.....	16
3.6.1 Circularity	22
3.6.2 Centroid Displacement.....	22
3.6.3 Area Difference.....	24
3.6.4 Fractal Dimension.....	25
3.7 Time Series Descriptors	26
4. ASSESSMENT.....	26
4.1 Classification of Possible Outcomes.....	28
4.2 Receiver Operating Characteristic Curves.....	29
4.3 Accuracy	31
4.4 Regression Models.....	32
4.5 Slice Classification Examples.....	36
5. STATIC DESCRIPTOR RESULTS.....	39
5.1 Circularity	39
5.2 Centroid Displacement.....	42
5.3 Area Difference.....	45
5.4 Fractal Dimension.....	48

5.5 Comparison of the Static Descriptors	51
5.7 Accuracy of the Static Descriptors	52
6. DYNAMIC DESCRIPTOR RESULTS.....	55
6.1 Centroid Dispersion	55
6.2 Percentage Change in Lumen Area.....	57
6.3 Comparison of the Time Series Descriptors	59
7. DISCUSSION.....	61
7.1 Misclassification	63
7.2 Combining the Descriptors	71
8. FUTURE WORK.....	73
9. SUMMARY	74
BIBLIOGRAPHY.....	75

List of Illustrations

Figures

Figure 1: The sections of the aorta.....	3
Figure 2: The layers of the artery wall.....	4
Figure 3: Plaque buildup causing narrowing of the artery lumen.....	5
Figure 4: Series of image slices from a cardiac CT scan.....	6
Figure 5: 3D reconstruction of the cardiac region from the CT scan illustrated in Figure 4....	7
Figure 6: 3D reconstruction of the section of the CT scan containing the aorta.	7
Figure 7: A heartbeat measured from the beginning of the R-wave when the A-V valve closes at the beginning of systole to the end of diastole.....	8
Figure 8: Full cardiac CT slice with a manually selected region of interest.....	15
Figure 9: Sample of selected input images.	15
Figure 10: PCNN model equations.....	17
Figure 11: Binary output images from the PCNN (a) and that output superimposed on the original image (b).....	19
Figure 12: The first three iterations of the binary output of the PCNN from Figure 11 summed to define the regions of interest.....	19
Figure 13: The lumen region selected from the image in Figure 12.....	20
Figure 14: The perimeter of the region in Figure 13.....	20
Figure 15: The estimated location of the lumen border superimposed on the original image.....	21
Figure 16: Perimeter calculation.....	21
Figure 17: The Hough circle center estimated from candidate center points.	23
Figure 18: The Hough circles outlined in green compared to the smallest enclosing circle. .	23
Figure 19: The estimated perimeter of the lumen with the smallest enclosing circle.....	24
Figure 20: Box counting of perimeter pixels.....	25
Figure 21: The slope of the line to estimate fractal dimension.....	25
Figure 22: Expert slice identification.....	27
Figure 23: Confusion matrix of possible outcomes for each discrimination threshold.	28
Figure 24: ROC Curve.....	30
Figure 25: The log odds compared to the regression estimate based on the circularity descriptor.....	33
Figure 26: Exponentiation of the log odds to yield the odds ratio at each level.....	33
Figure 27: The probability of plaque estimated based on the circularity descriptor.	34
Figure 28: Samples and descriptor values for images slices classified with indications of plaque.....	36
Figure 29: Samples and descriptor values for image slices classified as having no visible indications of plaque.....	37
Figure 30: Samples and descriptor values for image slices not classified.....	38
Figure 31: Samples of images slices in which a vessel branch (a) or another structure (b) prevents automated segmentation using the PCNN region output.	38
Figure 32: Circularity values.....	40
Figure 33: ROC curve for circularity.....	41
Figure 34: Percent difference values for the best estimate of the center of the artery and the centroid of the lumen.....	43

Figure 35: ROC curve for centroid displacement.	44
Figure 36: Percent difference in area between the lumen and the smallest enclosing circle containing the lumen.....	46
Figure 37: ROC curve for area difference.	47
Figure 38: Fractal dimension of the lumen perimeter.....	49
Figure 39: ROC curve for fractal dimension.	50
Figure 40: ROC Curves for all static descriptors.....	51
Figure 41: Accuracy of the circularity descriptor as the threshold varies.	53
Figure 42: Accuracy of the centroid displacement descriptor as the threshold varies.....	53
Figure 43: Accuracy of the area difference descriptor as the threshold varies.....	54
Figure 44: Accuracy of the fractal dimension descriptor as the threshold varies.....	54
Figure 45: Percentage change in the position of the lumen centroid at 0% to 40% of the R-R interval.....	56
Figure 46: ROC Curve for centroid displacement.	57
Figure 47: Percentage change in the area of the lumen at 0% to 40% of the R-R interval. ...	58
Figure 48: ROC Curve for area difference.	59
Figure 49: ROC Curves for time series descriptors.....	60
Figure 50: Accuracy measurements for the area difference descriptor.	62
Figure 51: The area of false negative slices.....	63
Figure 52: Image slices classified by physicians as having visual indications of plaque that would not be correctly classified by area difference descriptor.	66
Figure 53: The area of false positive slices.....	67
Figure 54: Image slices classified by physicians as having no visual indications of plaque that would not be correctly classified by area difference descriptor.	70

Tables

Table 1: Hounsfield Units for Representative Tissue Types	9
Table 2: Hounsfield Units for Plaque Characterization.....	10
Table 3: Input Datasets	13
Table 4: Classifier Comparison by Area under ROC Curve.....	52
Table 5: Accuracy Comparison	52
Table 6: Classifier Comparison by Area under ROC Curve.....	60
Table 7: Individual Logistic Regression Results	71
Table 8: Multiple Logistic Regression Result	71
Table 9: Reduced Multiple Logistic Regression Models.....	72

ABSTRACT

This study compared the ability of six image descriptors, characterizing the morphology and elasticity of the descending aorta, to identify computed tomography (CT) images which contain visual indications of plaque. This thesis is based on the hypothesis that regions of plaque distort the normal lumen shape resulting in corresponding changes in the CT image. This, in turn, allows the inference of the presence of plaque by identifying deviations in the smoothness, symmetry, or circularity of the lumen border or by measurements that allow for an estimate of the elastic properties of the arterial wall. The project method included manually locating the descending aorta from a CT dataset, segmenting the lumen in each candidate slice, and computing descriptors from the resulting images. The descriptors computed are the lumen circularity, lumen centroid displacement, the area difference between the smallest enclosing circle and the lumen border, and the fractal dimension of the lumen border. In addition, the percentage expansion in lumen area and the dispersion of the lumen centroid were compared at the 0% and 40% gating in the R-R interval during the cardiac cycle. An assessment of the ability of each descriptor to identify the image slices containing potential plaque is included. The descriptors were measured against a reference set of images which were visually classified by domain experts. While each of the calculated descriptors was shown to have some merit, the circularity and the area difference between the smallest enclosing circle and the lumen border demonstrated the best individual performances in discriminating between the plaque and non-plaque images. The overall best predictive model was found by combining the strengths of the two descriptors.

1. INTRODUCTION

Heart disease remains the leading cause of death in the United States, accounting for approximately 26.6% of the 2,450,000 deaths in 2005 [1]. In addition, cerebrovascular diseases such as stroke comprised an additional 5.9% [1]. Coronary artery disease is an underlying factor in the majority of cardiovascular disease cases [2]. The condition of the aorta is an indicator of vascular health. Specifically, studies have established that atherosclerosis of the thoracic aorta is one predictor for generalized atherosclerosis; coronary, carotid, and peripheral arterial disease [3].

1.1 Cardiovascular System

The cardiovascular system transports and distributes blood throughout the body to deliver materials such as oxygen and nutrients and to carry away waste products. The blood vessels form a closed transport system with the arteries carrying blood away from the heart. The large elastic arteries leave the heart and help propel blood. During ventricular contraction, their elasticity acts to accommodate the surge of blood and helps to maintain an even pressure [4].

The aorta is the largest elastic artery with a typical diameter of 2-3 centimeters [4]. The aorta is described by sections: the ascending aorta, the aortic arch, and the descending aorta. As illustrated in the diagram shown in Figure 1, the ascending aorta emerges from the left ventricle of the heart with the coronary arteries branching from it to supply the heart muscle. The aorta curves to form the aortic arch which is the transverse segment containing branches to supply the head, neck, and upper limbs. The aortic arch completes an approximately 180° turn at which point the aorta descends along the spine. The descending portion is referred to as the thoracic aorta above the diaphragm and the abdominal aorta below [4] [5].

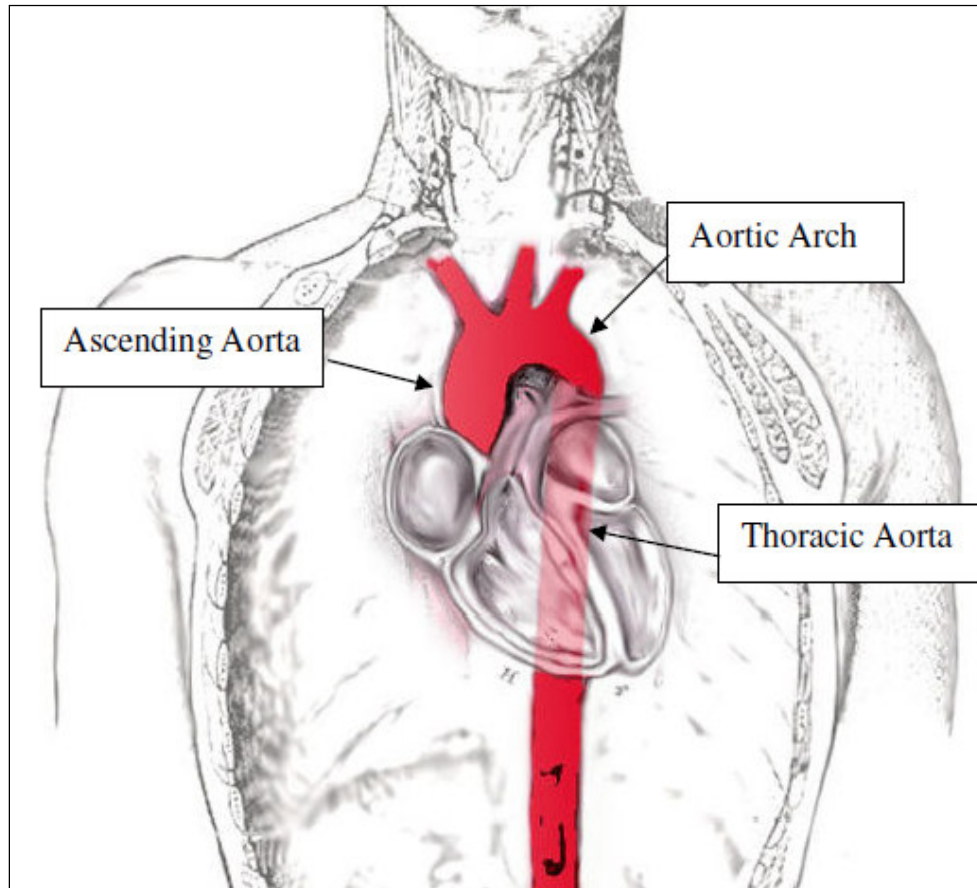


Figure 1: The sections of the aorta [6].

As shown in Figure 2, the wall of an artery has three tunics or layers; the tunica interna, the tunica media, and the tunica externa. The interna or intima is the inner surface closest to the lumen, the hollow center through which blood flows. The interna contains a lining composed of a continuous layer of cells called the endothelium, the tissue which makes contact with the blood [4]. It is surrounded by a sub-layer of connective tissue interlaced with circularly arranged elastic bands. The media is the thickest layer made of elastic fiber, connective tissues, and polysaccharide. It is separated from the third, outermost layer by another elastic layer. The outer layer, or adventitia, is made of connective tissue and contains nerves and capillaries.

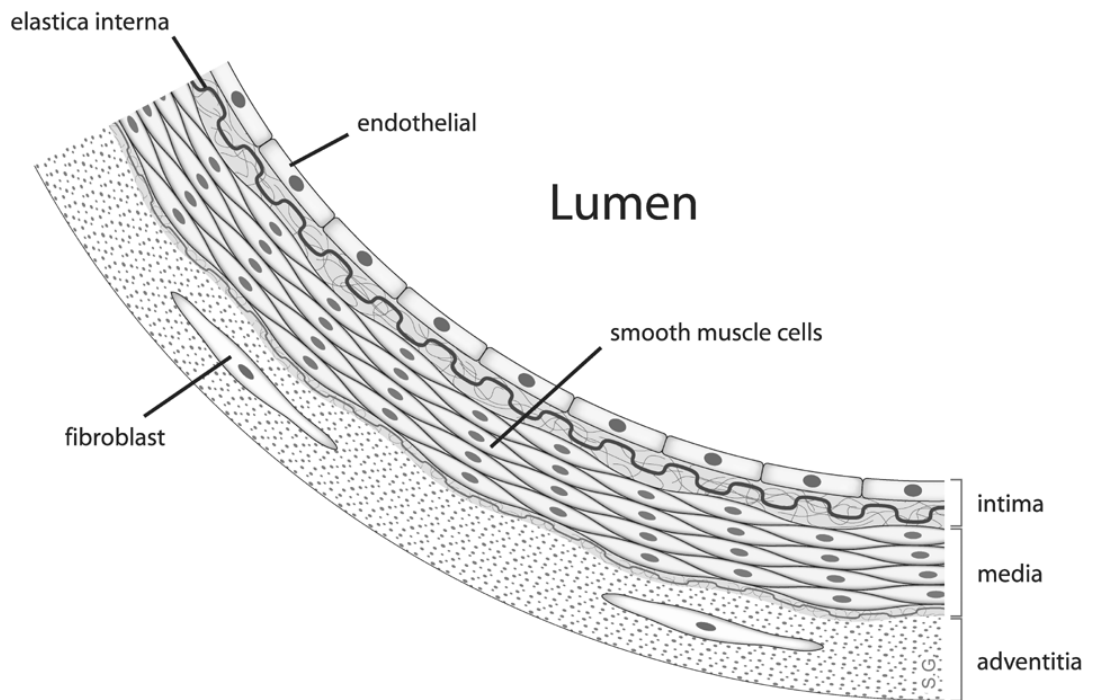


Figure 2: The layers of the artery wall [7].

1.2 Atherosclerosis

Arteriosclerosis is the thickening of the artery walls and the loss of elasticity. One form of arteriosclerosis, atherosclerosis, is believed to begin with damage to the endothelium.

Risk factors for atherosclerosis include:

- elevated cholesterol and triglyceride levels in the blood
- high blood pressure
- smoking
- diabetes [8]

Damaged sites collect fat, cholesterol, calcium, cellular waste products, and other substances found in the blood along the arterial wall as illustrated in Figure 3 [9]. This buildup is called plaque, and it may thicken the endothelium significantly [8]. The severity of the atherosclerosis is often characterized by the amount and structure of the observed plaque. A plaque is generally defined as a protrusion of the intimal surface of the vessel at least 2 mm thick which is different in appearance from the intimal surface.

Plaques less than 4mm are considered small while those greater than or equal to 4 mm are classified as large or severe [10] [11]. Ulceration, a discrete indentation of the luminal surface of the plaque with base width and maximum depth of at least 2 mm, can also occur [11]. In addition, approximately 90% of patients with cardiovascular disease exhibit vascular calcifications. These deposits of calcium hydroxyapatite, a natural component found in bones and teeth, can diminish the wall elasticity [12] necessary for pressure regulation.

Litovchik et al described the strong relationship between coronary, carotid, and aortic calcification in studies including the study of Eisen et al of a high risk population in which 91% of patients had coronary calcification. Of these patients, 70% also had aortic calcification [5].

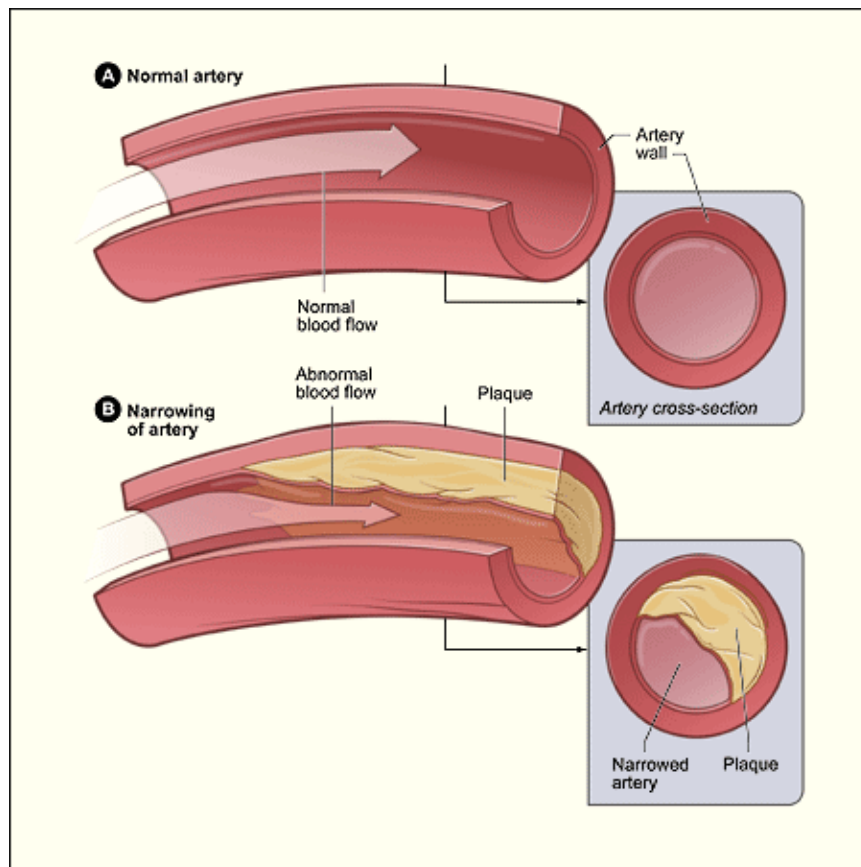


Figure 3: Plaque buildup causing narrowing of the artery lumen [9].

1.3 Computed Tomography

Computed tomography (CT) has become a mainstay of non-invasive imaging for vascular anatomy and pathology and is a common method for diagnosing vascular disease [5]. In a CT scan, an X-ray source rotates around the target to produce a set of cross-sectional images, or slices [13]. A subset of image slices from a cardiac CT scan is shown in Figure 4. This series of CT slices can be used to reconstruct a 3D model of the internal structures as illustrated in Figure 5 [14].



Figure 4: Series of image slices from a cardiac CT scan.

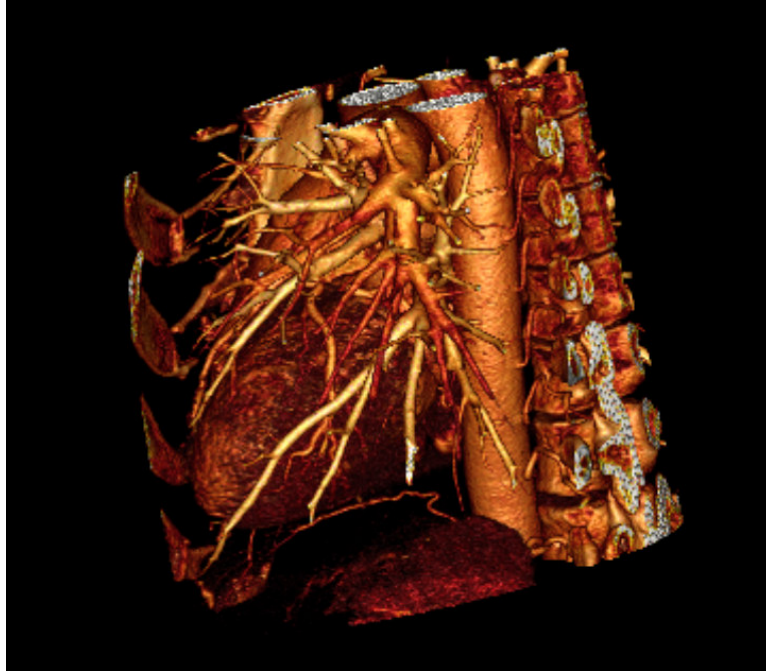


Figure 5: 3D reconstruction of the cardiac region from the CT scan illustrated in Figure 4.

In particular, this study is focused on individual slices selected from the area of the descending aorta as illustrated in the reconstruction in Figure 6.



Figure 6: 3D reconstruction of the section of the CT scan containing the aorta.

In addition to still or static volumes, CT scanners can acquire motion sequences by synchronizing, or gating, image acquisition to the cardiac cycle. These CT scanners are typically gated as an offset referenced to the R-R interval in an electrocardiogram. The cardiac cycle refers to the sequence of events relating to the pressure and flow of blood from the beginning of one heartbeat to the beginning of the next. As shown in Figure 7, one beat is generally measured from the peak of one R-wave, when the atrioventricular (A-V) valve closes, to the peak of the next. Figure 7 also illustrates the changes in aortic pressure during the cardiac cycle which form the basis for the elastic descriptors described later in this thesis.

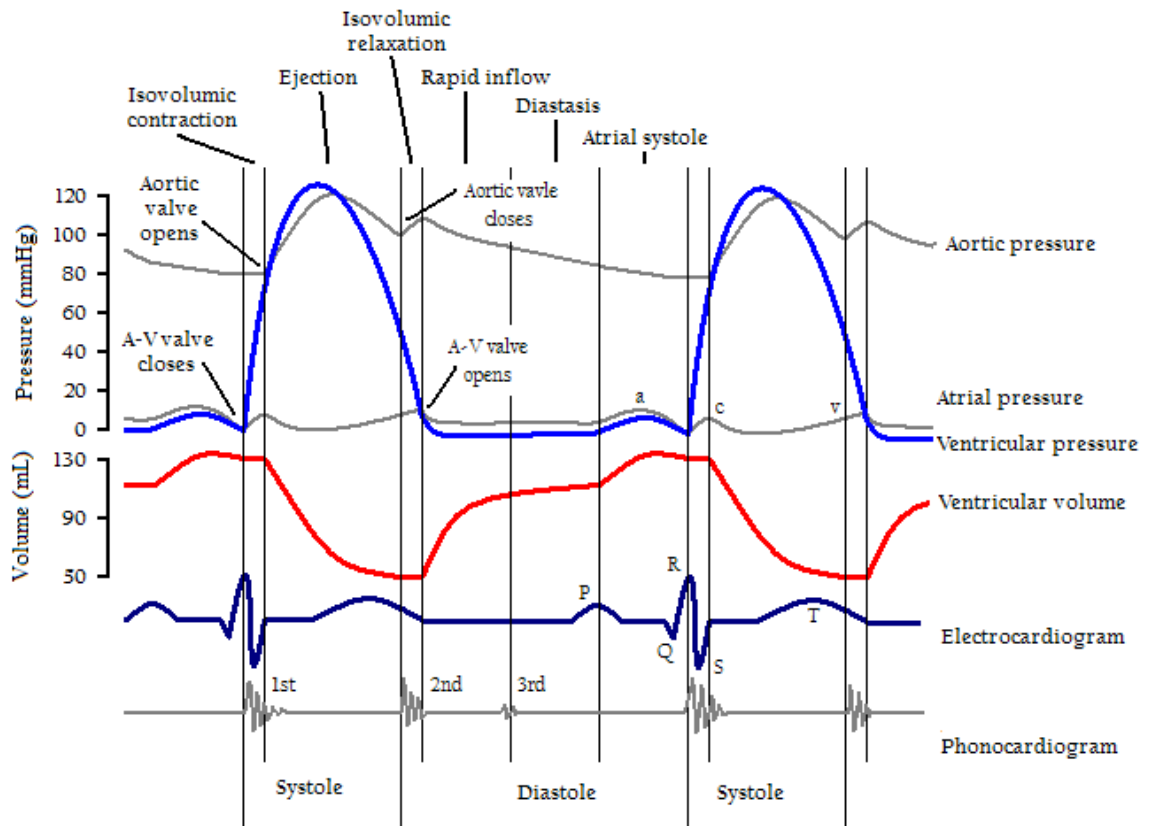


Figure 7: A heartbeat is measured from the beginning of the R-wave when the A-V valve closes at the beginning of systole to the end of diastole [15].

The gating effectively divides the R-R interval into a number of segments, usually between 10 and 20. Each reconstructed CT volume relies on data obtained at a fixed offset in the cardiac cycle. For consistency, the static descriptors in this study are all based on the CT images taken at the 75% point in the cardiac cycle; that is, 75% of the time of one heartbeat measured from the beginning of the R-wave. For the time series descriptors, calculations are based on the differences between the images obtained at 0% (the beginning of the R-wave) and 40 % of the cardiac cycle.

Tissue densities in CT images are recorded in terms of Hounsfield Units (HU). In a CT scan, an arbitrary unit of x-ray attenuation is assigned to each voxel on a scale in which air has a value of -1000 HU; water, 0 HU; and compact bone, +1000HU. Values for Hounsfield Units are shown in Table 1 for representative tissue types [16]. The HU scale is from -1,024 to +3,071, a 12-bit range or grayscale of 4,096 from jet black (-1,024 HU) to pure white (3,071 HU).

Since soft plaque is substantially transparent to x-ray, a contrast agent is used to allow better visualization of plaque-related lumen displacement [12]. Schroeder et al compared plaque compositions in contrast enhanced CT scans with results found by intracoronary ultrasound to define plaque density ranges as shown in Table 2 [17].

Table 1: Hounsfield Units for Representative Tissue Types

Tissue	Hounsfield Units
Bone	1000
Liver	40 to 60
White Matter	~20 to 30
Grey Matter	~37 to 45
Blood	40
Muscle	10 to 40
Kidney	30
Cerebrospinal Fluid	15
Water	0
Fat	-50 to 00
Air	-1000

Table 2: Hounsfield Units for Plaque Characterization

Estimated Range	Actual Range	Plaque Characterization
14 ± 26 HU	-42 to +40 HU	soft plaque
91 ± 21 HU	61 to 112 HU	intermediate plaque
419 ± 194 HU	126 to 736 HU	calcified plaque

Nandalur et al used similar definitions for plaque density [18]. Their study defined soft plaques with lipid rich cores as having median density less than 50 HU; intermediate plaques, associated with large amounts of fibrous tissue, having densities of 51-130 HU; and calcified plaques as having densities above 130 HU. They also observed that calcified plaques generally had densities considerably higher than 350 HU which is the median density of contrast media.

2. LITERATURE REVIEW

2.1 Image Segmentation

Kurkure, Avila-Montes, and Kakadiaris [19] developed a method to locate and segment the thoracic aorta in non-contrast CT images to replace the manual annotation of calcified plaques. Their method used a series of 2D slices from the CT data based on the assumption that the aorta runs approximately vertically in this section of the abdomen. After preprocessing, they applied a Hough circle transform on regions of interest for the ascending and descending aorta and they found an optimal combination of the Hough circles by using a cost function which minimized the change in horizontal position between circles in adjacent slices, the change in radius between circles in adjacent slices, and the Hough value of points in Hough space. An additional cost function was able to further refine gaps and smooth out the horizontal boundary. Their segmentation method compared favorably when it was evaluated against aortic boundaries manually annotated by an expert. Consistent with the Kurkure method, this project takes advantage of the relatively vertical orientation of the descending aorta and processes the subset of image slices with the assumption that the 2D cross-section of the aorta is approximately circular. Both the circularity descriptor and the measurement of the displacement of the centroid from the artery center are based on this assumption.

Renard and Yang [20] developed a technique for segmenting both the lumen and the arterial wall in contrast-enhanced CT images of the coronary arteries by determining a centerline and classifying the tissues within a cylinder centered on that line. They separated the tissues into lumen, wall, and the surrounding myocardium and noted that the lumen intensity was the brightest among the three classes. The difference in the cross-sectional areas of the lumen and the wall regions was then used to estimate plaque regions. This thesis also relies upon the brightness of the contrast-enhanced lumen to distinguish its border from the surrounding tissues, concentrating on characteristics of the lumen border outline to indicate potential plaque areas.

2.2 Image Descriptors

Once the lumen boundary has been estimated, its characteristics can be described. Nguyen, and Rangayyan [21] found that the fractal dimension was a good shape feature to quantify the complexity and irregularity of an object's boundary. The technique was successfully applied to contours that were hand drawn by an expert on over 100 mammogram masses, and a clear separation of benign and malignant masses was found, with the smoother contours of the benign masses generating a lower fractal dimension. In a similar way, the presence of plaque was expected to increase the complexity and irregularity of the lumen border which would be reflected in a higher calculated fractal dimension.

In addition to static descriptors to identify image slices containing potential areas of plaque, information about the elastic properties of the aortic wall from time series images is explored. These images are recorded at increments within the R-R interval, the duration of the cardiac cycle. Stefanadis et al [22] verified that aortic elastic properties represent a substantial independent risk factor in predicting coronary events in patients with coronary artery disease. They considered distensibility, calculated from the percentage change in cross-sectional area between diastole and systole, in evaluating elastic properties. Galante et al [23] segmented the aorta from multi-detector CT images and estimated shape and size features using a temporal resolution of ten frames per cardiac cycle. They were able to verify a decrease in elasticity and strain in vessels

containing aneurysms, and their measurements compared well with current methods which require doctors to perform manual measurements of aortic diameters at specific anatomical sites. This thesis considers the percentage expansion of the lumen as an indicator of distensibility and the dispersion of the centroid value as a measure of asymmetry to determine how the presence of plaque might be associated with stiffness or asymmetry in the expansion of the aortic cross-sectional area during the cardiac cycle.

3. METHODOLOGY

3.1 Overview

The focus of this study is a comparison of the ability of a set of descriptors to characterize images of the aorta to identify those with potential areas of plaque. The method required:

- Manual selection of a region of interest containing the descending aorta from a complete CT scan.
- Segmentation of the lumen border outline:
 - Initial highlighting of the region of lumen candidate pixels using a pulse-coupled neural network (PCNN).
 - Identifying the outer border of this region of interest.
- Calculation of descriptors based on border outline of a single image obtained at the 75% gating of the cardiac cycle. These are referred to as “static descriptors” and include:
 - Circularity based on perimeter and area of lumen.
 - Difference between the best estimate of the center of the artery and the centroid of the lumen.
 - Percentage difference between the lumen area and the area of the smallest enclosing circle containing the lumen area.
 - Fractal dimension of the border outline.

- Incorporation of time series information into “dynamic descriptors” comparing differences in image slices recorded at 0% and 40% gating during the cardiac cycle including:
 - Dispersion of the centroid value as a measure of asymmetry in aortic expansion.
 - Distensibility based on the percentage expansion of the area of the lumen.
- Comparison of the ability of each descriptor to identify the subset of image slices containing potential plaque areas that have been validated by a medical expert.

A review of the resources used and a detailed explanation of each step are contained in the following sections.

3.2 Datasets

The project analyzed 768 slices from eight CT studies manually classified by domain experts under the direction of Jeffrey Soble, M.D., Associate Professor of Medicine, Chief of Cardiology Clinical Consultant Service, Associate Director, Clinical Echocardiography, and Director, Cardiology Information Services at Rush University Medical Center, Chicago, Illinois. Additional information on the classifications may be found in section 4, Assessment. Of these 768 slices, 168 slices were identified as likely to be atherosclerotic and 600 were found to have no visually detectable indications of plaque. In addition there were 34 images which the experts declined to classify for a total of 802 images. A summary of the dataset features is shown in Table 3.

Table 3: Input Datasets

Manufacturer	Model Name	Station Name	Series Description	Rows	Cols	Slice Thickness	Pixel Spacing		Plaque	Non-Plaque
Philips	Brilliance 64	philips-9502	75%	512	512	0.90	0.400391	0.400391	45	29
Philips	Brilliance 64	philips-9502	75%	512	512	0.67	0.386719	0.386719	0	8
Philips	Brilliance 64	philips-9502	75%	512	512	0.90	0.429688	0.429688	22	162
Philips	Brilliance 64	philips-9502	75%	512	512	0.90	0.507822	0.507822	0	73
Philips	Brilliance 64	philips-9502	75%	512	512	0.67	0.300781	0.300781	0	131
Philips	Brilliance 64	philips-e4cd175	75%	512	512	0.90	0.359375	0.359375	0	197
Philips	Brilliance 64	philips-9502	75%	512	512	0.67	0.429688	0.429688	46	0
Philips	Brilliance 64	philips-9502	75%	512	512	0.67	0.429688	0.429688	55	0

3.3 Software Summary

A variety of open source software packages were supplemented by custom programming to process the CT datasets, including the following:

- OsiriX: an image-processing software package which is compliant with the DICOM format, the standard for producing, storing, and displaying medical images. It was designed for the visualization of multidimensional images and contains 2D, 3D, and 4D viewers. It can read and display DICOM format files as well as the DICOM meta-data contained in the file headers. In addition, it can write a DICOM file from a 2D/3D reconstruction which allowed manual inspection and selection of a volume of interest from the full CT scan dataset [14].
- The Insight Toolkit (ITK): modules for performing registration and segmentation of medical images. It also provides the ability to read and write a DICOM format file, and it contains numerous filtering, geometric transformation, and statistical functions. It is primarily a C++ package, but many of the functions have been wrapped for alternative programming languages such as Python [24].
- Other available tools: Python and NumPy to process multidimensional arrays, SciPy for scientific applications, and the Visualization Toolkit (VTK) for 2D and 3D visualization [25].
- Custom software developed for PCNN pre-processing [26] [27].

3.4 Selection

The descending thoracic section of the aorta can be roughly selected from the complete CT scan dataset as a volume of interest to facilitate and minimize the amount of processing required. As in the Kurkure study [19], the analysis takes advantage of the relatively vertical orientation of the descending aorta, resulting in a series of 2D image slices in which the cross-section of the aorta is approximately circular. Figure 8 is an example of one full CT slice in which the region of interest, including the descending aorta, is identified by the green rectangle. In each study, the region of interest containing the descending aorta was manually selected and propagated through the individual slices from a complete CT scan. The resulting volume of interest was written to a new DICOM file.

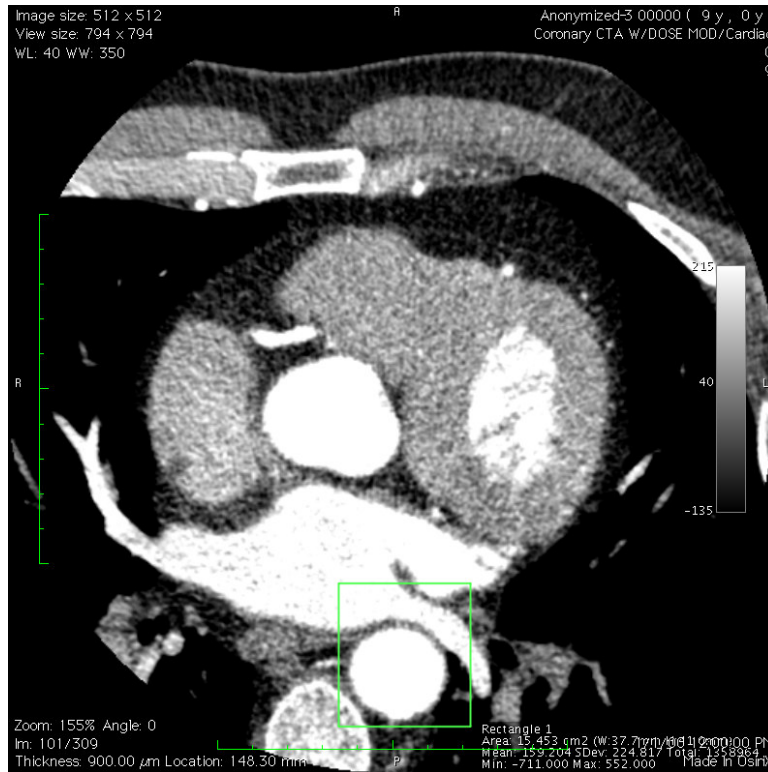


Figure 8: Full cardiac CT slice with a manually selected region of interest.

For the static descriptors, this volume of interest contained between 200 and 300 slices in the series taken at 75% of the R-R interval. Figure 9 shows a sample of regions of interest. From this volume subset, usable image slices were selected based on the ability to segment the lumen of the aorta without interference from branching vessels or other anatomical structures with HU values similar to that of the contrast agent.

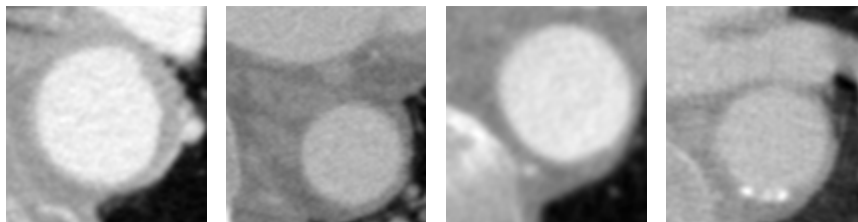


Figure 9: Sample of selected input images.

The study images, as shown above, were converted from the DICOM format to TIFF which is a flexible public domain raster file format originally developed by Adobe for archiving images [28]. Since this process simply added a constant offset of 1024 to the HU value of each pixel, it allowed for visual inspection of the results at each stage of the process without any gain or loss of image information.

3.5 Segmentation

To help identify the lumen, each image was preprocessed by a pulse-coupled neural network (PCNN) [29]. The output of a PCNN is a series of pulses or binary images associated with visually interesting features and boundaries. In contrast to some other neural networks such as the multi-level perceptron, the PCNN does not use multiple layers (input, hidden, output) nor does it involve training [30]. This model involves only a single layer with the connections between a neuron and its neighbors based on the distance between their positions [30]. The segmenting and edge detection ability of the PCNN is derived from the influence of a neuron on its neighbors which encourages similar segments of the image to pulse in unison [30] [31] [32]. The PCNN has been used successfully as a pre-processing step in other medical imaging applications which required segmentation of borders or tissue types [26] [27] [33] [34].

The PCNN is modeled after the processing of the visual cortex in a small mammal. This is the part of the brain that receives processed information from the eye and converts it into a stream of pulses. Eckhorn used the cat visual cortex to develop a neuron model [35] which was adapted for image processing by Lindblad and Kinser [29]. Their resulting computer model retains two important characteristics of the biological system:

- The neurons or visual receptors are interconnected meaning that when one receptor receives optical input, it affects the behavior of its neighbors.
- The eye receives feedback information which affects the output of a receptor.

$$\begin{aligned}
F_{ij}(t) &= e^{-\alpha_F \delta t} F_{ij}(t-1) + S_{ij} + V_F \sum_{kl} W_{ijkl} Y_{kl}(t-1) \\
L_{ij}(t) &= e^{-\alpha_L \delta t} L_{ij}(t-1) + V_L \sum_{kl} M_{ijkl} Y_{kl}(t-1) \\
U_{ij}(t) &= F_{ij}(t)(1 + \beta L_{ij}(t)) \\
Y_{ij}(t) &= \begin{cases} 1 & \text{if } U_{ij}(t) > \theta_{ij}(t-1) \\ 0 & \text{otherwise} \end{cases} \\
\theta_{ij}(t) &= e^{-\alpha_\theta \Delta t} \theta_{ij}(t-1) + V_\theta Y_{ij}(t)
\end{aligned}$$

Figure 10: PCNN model equations.

Lindblad and Kinser’s model, detailed in Figure 10, has been used successfully in image processing with desirable features that include relative immunity to translation, scaling, and rotation [29]. In their PCNN model, each image pixel serves as the input stimulus value “ S ” for the individual neuron at position ij and has the following properties at each pulse:

- Every neuron receives feeding input “ F ” based on its own stimulus and those of neighboring neurons.
- Every neuron receives linking input “ L ” based on output from other neurons.
- The feeding and linking input components are combined to form an activity term “ U ” for the neuron which is compared to a threshold to determine the binary output, “ Y ”, of the neuron at interval t .
- The threshold “ θ ” decays with each pulse until the neuron activity level exceeds the threshold value and fires. The neuron firing also causes “ θ ” to be reset to its highest point.
- “ M ” and “ W ” represent weighting factors for the inputs in the feeding and linking functions.

The parameters used in this study were chosen empirically as:

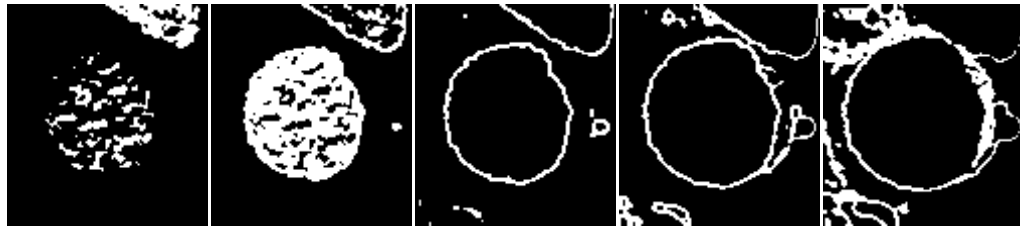
- α -values for the feeding, linking, and threshold were set at 10.0, 1.0, and 15.0.
- The β value for the strength of the linking term in the activity calculation was 0.1.
- The V-potential values for feeding, linking, and resetting the threshold were set at 0.0, 0.5, and 20.0.

In addition, the initial threshold θ and the value of $Y(t - 1)$ were set to zero for each neuron.

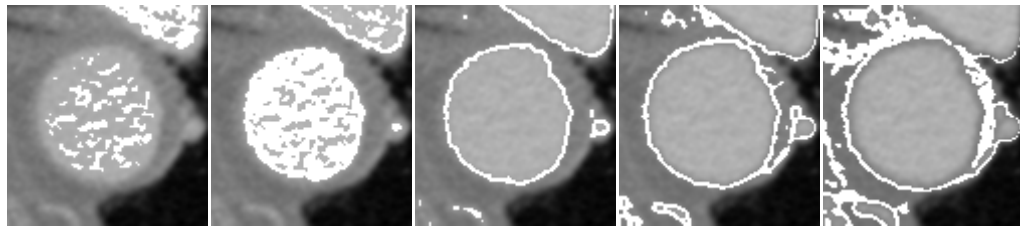
For each set of study images, a representative image slice was selected for input in a preliminary execution of the PCNN. The pixel values were contrast-stretched from a range of approximately 0 to 2000 to a range of 0 to 65535. Fifty iterations of the PCNN were executed in the trial, resulting in a series of binary images. A subset of these binary images is shown in Figure 11 along with this binary output superimposed on the original image for reference. The output from the representative image was used to visually select the iteration that best outlines the lumen border.

It was observed that due to the high HU value of the lumen area, early pulses begin within the lumen and propagate out toward the border before breaking up. This auto-wave, characteristic of the PCNN [30], allowed the creation of a binary map of the lumen region by summing the PCNN output for a fixed number of iterations as illustrated in Figure 12. Other features in the image also have pulse output from the PCNN so the lumen area must be separated from this binary output as shown in Figure 13.

The perimeter of the region of interest forms the estimated location of the lumen border as shown in Figure 14. This estimated border is defined by the set of pixels which have a background pixel (black) in a 4-neighbor as illustrated by Burger and Burge [36]. This calculated border is superimposed on the original image for illustration in Figure 15. The lumen perimeter and region area serve as the basis for calculating the static image descriptors which are described in the subsequent sections.



(a)



(b)

Figure 11: A subset of binary output images from the PCNN (a) and that output is superimposed on the original image (b).

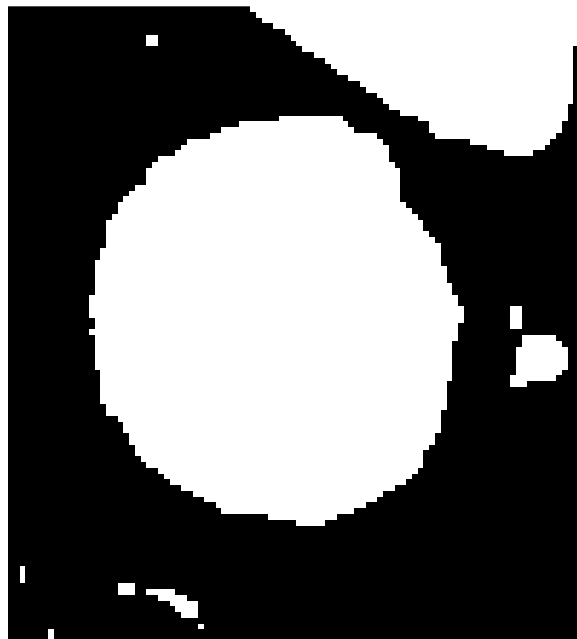


Figure 12: The first three iterations of the binary output of the PCNN from Figure 11 are summed to define the regions of interest.

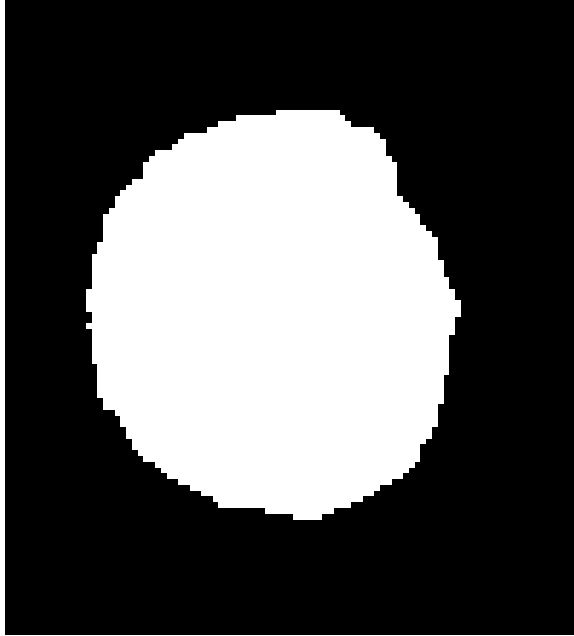


Figure 13: The lumen region is selected from the image in Figure 12.

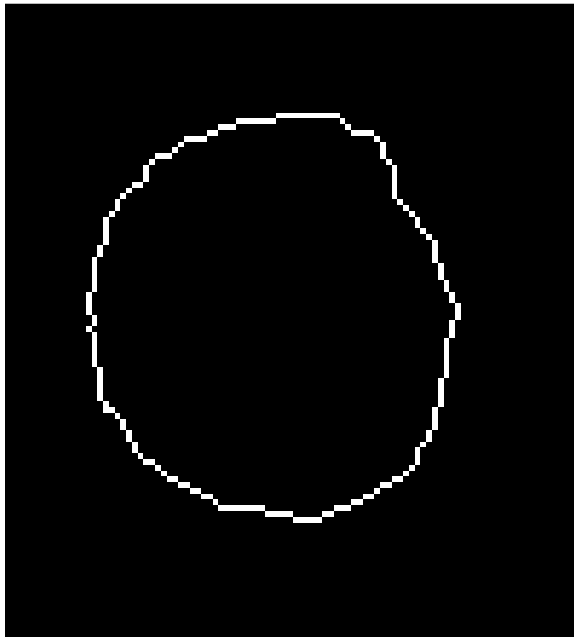


Figure 14: The perimeter of the region in Figure 13 is segmented.

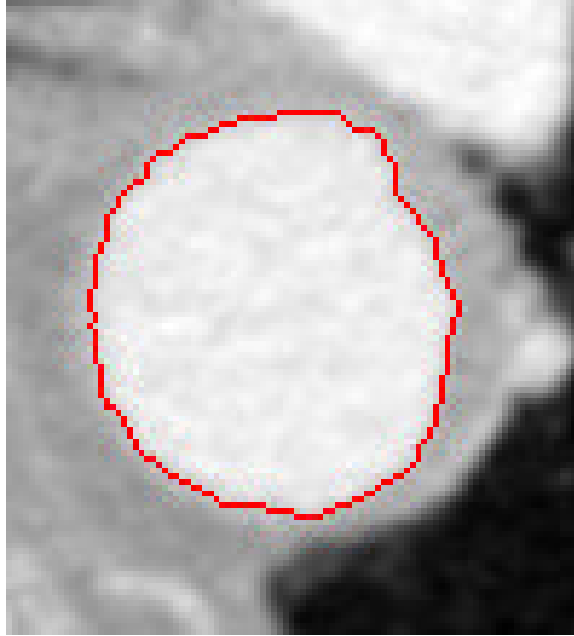


Figure 15: The estimated location of the lumen border superimposed on the original image.

3.6 Static Image Descriptors

The static descriptors computed are the lumen circularity, lumen centroid displacement, the area difference between the smallest enclosing circle and the lumen border, and the fractal dimension of the lumen border. The descriptors were computed for each individual image slice.

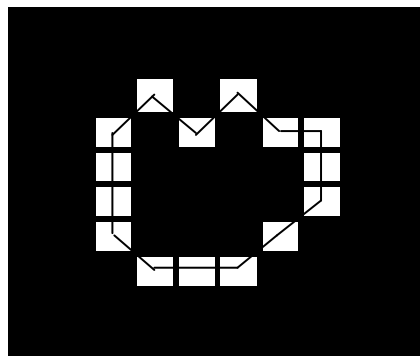


Figure 16: Perimeter calculation

$$perimeter = .95 \times (5vertical + 3horizontal + \sqrt{2} \times 7diagonal) = 17.0$$

3.6.1 Circularity

The first descriptor calculates the lumen border perimeter and the area of the lumen to form an estimate of circularity. As illustrated in Figure 16, the perimeter measurement is estimated by the length of the outer contour of the connected region R . Each segment measures the distance from one pixel center to an adjoining pixel center. The measurement estimates vertical and horizontal segments as 1 unit and diagonal segments by $\sqrt{2}$ units. Since this method of calculation has been generally found to overestimate the real perimeter, a correction factor of 0.95 is applied as recommended in [36]. The area estimation is a simple count of the image pixels that comprise the region R . Circularity can be approximated from the perimeter and the area as a measure of compactness or roundness which is invariant to translation, rotation, or scale factors:

$$Circularity(R) = 4\pi \times \frac{Area(R)}{Perimeter^2(R)}$$

Circularity is 1 for a perfectly round region and ranges from [0, 1) for all other shapes [36].

3.6.2 Centroid Displacement

The second descriptor considered was the distance between the centroid of the lumen and the center of the best circle fit to the lumen outline, expressed as a fraction of the radius. A preliminary feasibility study explored using a Hough circle transform to calculate the circle. The Hough circle transform is potentially robust even under conditions which occlude parts of an image boundary as illustrated in Figure 17. This is in contrast to the centroid which can be moved away from its central position by defects or boundary occlusions [37]. The Hough transform creates a set of candidate points for the center of a circle (or circles), given a radius value (or range of values), by moving along the local normal vector for each point on the perimeter. The location(s) containing the largest number of accumulated candidate points defines the center of the best fit circle(s). In practice, for this application, the Hough transform did not provide a consistent reference to the center of an artery because the radius value was variable and the circle was not constrained to contain all of the points of the lumen border. As illustrated in Figure 18, the Hough circles did not consistently outline an artery to distinguish the areas of

potential plaque. Ultimately, the smallest enclosing circle containing the lumen area proved to be a more reliable estimate of the arterial center.

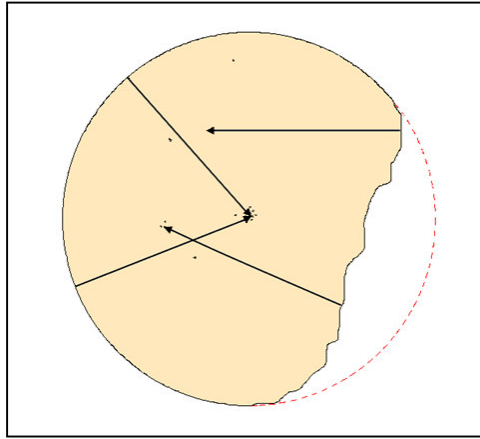
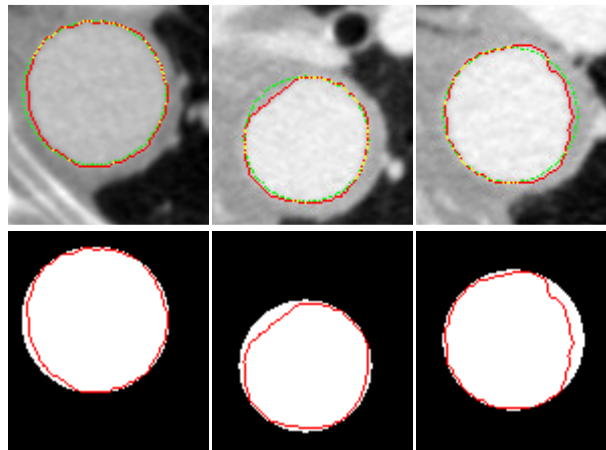


Figure 17: The Hough circle center estimated from candidate center points.



(a) non-plaque (b) borderline (c) plaque

Figure 18: The Hough circles outlined in green (top row) compared to the smallest enclosing circle (bottom row).

This constructed enclosing circle is compared to the Hough circles in Figure 18 and is illustrated in detail in Figure 19. As described by Schneider and Eberly [38], the algorithm used to determine the minimum area circle begins with a circle that contains two input points and “grows” a circle that contains all of the points. After constructing a circle with the first two support points, all additional points must be tested for inclusion in the circle. If all of the points are contained, the minimum area circle has been found. Otherwise, the first non-contained point is added to the list of support points and all

circles that can be constructed from the combinations of two or three support points must be found. The selected “grown” circle is the minimum area circle that has been constructed which contains all of the old supporting points. This circle is then tested to see if it contains all of the input points. Again if all of the additional points are contained, the minimum area circle has been found. If not, any previous supporting points which are now interior points must be removed from the support list and the algorithm must be restarted.

The center of this enclosing circle was then used in the second descriptor to estimate the difference between the center of the artery and the centroid of the lumen.

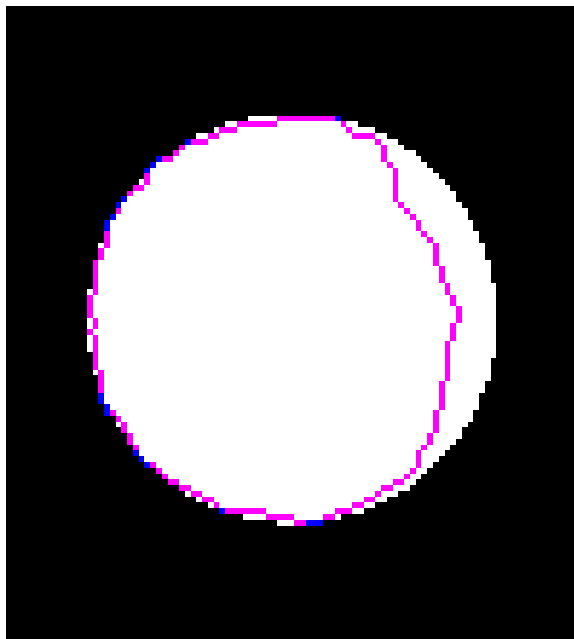


Figure 19: The estimated perimeter of the lumen is shown in magenta with the smallest enclosing circle highlighted in white. The blue pixels directly intersect the circle border.

3.6.3 Area Difference

The enclosing circle, calculated for the centroid displacement descriptor and illustrated in Figure 19, was also used to estimate the occlusion of the artery by calculating the percentage difference between the calculated lumen area and the area of the smallest enclosing circle.

3.6.4 Fractal Dimension

The final static descriptor is the fractal dimension as described by Nguyen and Rangayyan [21] which quantifies the complexity of the lumen boundary. The fractal dimension was calculated using the box-counting method. For the case of the lumen perimeter, the method partitions the image into a grid of squares of equal size and counts the number of squares that contain at least one perimeter pixel as illustrated in Figure 20. Grid size is then varied from one square pixel to 64 square pixels. The fractal dimension is estimated by the slope of the line found for a linear regression of the log of the number of boxes containing lumen border pixels and the log of the magnification index for each box-partitioning stage. Figure 21 is a graph showing the estimate of fractal dimension for the image in Figure 20.

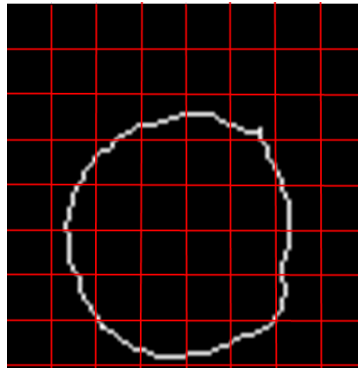


Figure 20: For this grid size, 20 boxes contain perimeter pixels.

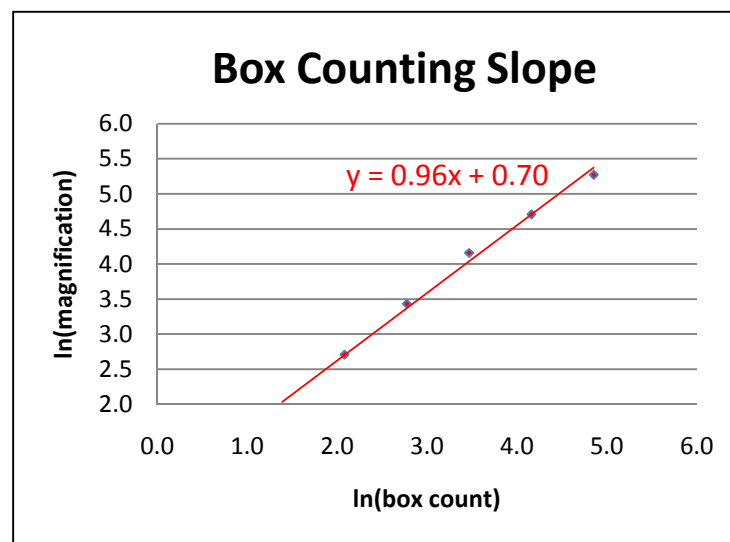


Figure 21: The slope of the line estimates the fractal dimension of the perimeter outline shown in Figure 20.

3.7 Time Series Descriptors

As in the studies by Galante et al and by Stefanadis et al [22] [23], an alternative to static image descriptors is an estimate of the elastic properties of the aorta using images obtained throughout the cardiac cycle. These descriptors are calculated for the series in the study which contain slices acquired at 0% and 40% gating, expressed as a fraction of the R-R interval in the cardiac cycle. The difference in the centroid values is calculated as a measure of asymmetry in aortic expansion. In addition, the percentage change in the area of the lumen at systole and diastole is used to estimate a measure of distensibility.

4. ASSESSMENT

The static descriptors compared in this study are the circularity of the lumen outline, the distance between the centroid of the lumen and the center of the smallest enclosing circle, the area difference between the smallest enclosing circle and the lumen, and the fractal dimension of the lumen outline. In addition, dynamic descriptors include the dispersion of the centroid values and the percentage change between the area of the lumen at systole and diastole which are evaluated for studies having the time series data available. The descriptors are evaluated for their ability to identify slices which contain potential areas of plaque.

A “gold standard” is defined as the true disease status, measured without error. It may be defined from clinical follow-up, surgical validation, or autopsy [39]. In the absence of an available, non-invasive “gold standard”, and consistent with other studies [19] [20] [23], the descriptors for this study are assessed against the evaluation of domain experts. As illustrated in Figure 22, two cardiologists evaluated each slice and identified it as either containing visible indications of plaque, or as normal, or they declined to classify the slice. For example, the slice image in Figure 22(b) shows two indications of plaque, both soft plaque distorting the arterial border and calcification indicated by the higher intensity pixels on the lower right aorta border.

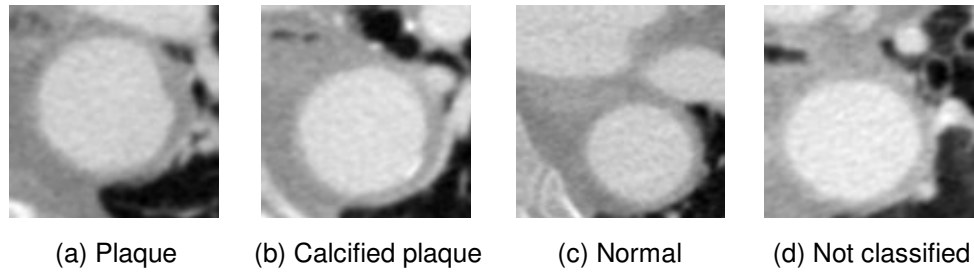


Figure 22: Expert slice identification.

To minimize assessment error, this study is restricted to images classified identically by two cardiologists. The resulting set of classified images is designated as the “reference set” for the balance of this thesis.

The assessment tools used for this thesis include Receiver Operating Characteristic curves, accuracy measurements, and logistic regression analysis. These are elaborated in the following sections.

4.1 Classification of Possible Outcomes

The descriptors have been calculated from classification models that map each slice instance to a continuous value. A threshold can then be applied to this value to predict membership in the plaque or non-plaque classes. For each descriptor and slice instance value, there are four possible outcome combinations as shown in Figure 23. This matrix of possible outcomes is referred to as a confusion matrix or a contingency table [40].

		<u>True Class</u>	
		plaque	non-plaque
<u>Predicted Class</u>	plaque	true positive	false positive
	non-plaque	false negative	true negative

Figure 23: Confusion matrix of possible outcomes for each discrimination threshold.

The true positive rate or sensitivity of a test can be estimated by:

$$\text{true positive rate} = \frac{\text{true positives}}{\text{total positives}}$$

The specificity of a test is also called the true negative rate. The false positive or false alarm rate is equal to (1-specificity) and is estimated by:

$$\text{false positive rate} = \frac{\text{false positives}}{\text{total negatives}}$$

4.2 Receiver Operating Characteristic Curves

One method that this thesis uses to report results is the Receiver Operating Characteristic (ROC) curve which characterizes their respective sensitivity and specificity. The area under the ROC curve is estimated to assess the potential of each descriptor [41].

As illustrated in Figure 24, the ROC graph illustrates the tradeoff between the true positive rate and the false positive rate of a classifier or descriptor. The ROC graph is a plot of the true positive rate on the y-axis against the false positive rate on the x-axis as the discrimination threshold for the descriptor values varies from $-\infty$ to $+\infty$. In ROC space, the point (0, 0) is the state of never classifying an instance as positive and therefore has no chance of a false positive error. The point (1, 1) unconditionally classifies all instances as positive so all negatives will be classified incorrectly as false positives. The diagonal line represents a classifier that has no more information than randomly guessing a class. The point (0, 1) represents a perfect classifier. Intuitively, a classifier point is better if it is closer to the (0, 1) corner which means that either the true positive rate is higher, the false positive rate is lower, or both. By varying the classifier threshold for the continuous values that are produced by the descriptors, a curve (step-function) in the ROC space is produced [40].

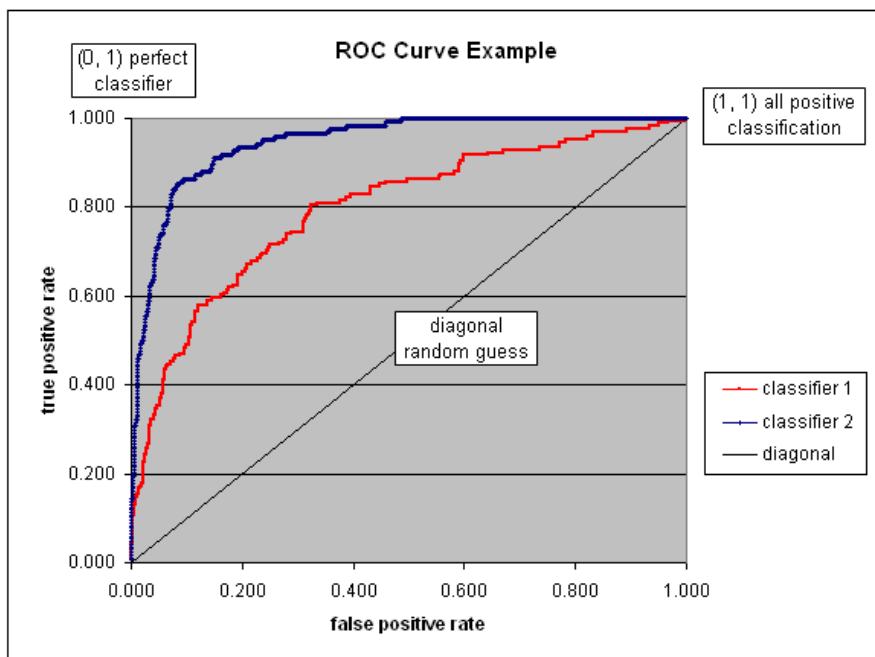


Figure 24: ROC Curve.

One positive property of a ROC curve is that if the proportion of positive to negative instances changes in a test set, the curve will not change since it depends only on the true positive and false positive rates [40].

Since a successful classifier will produce relative scores or values to discriminate normal and abnormal instances of the test outcome [40], the area under an ROC curve (AUC) will vary from .5 which indicates no predictive value to 1.0 representing perfect accuracy. The area measures the probability that in a random pair consisting of a normal and an abnormal image, the descriptor will allow them to be correctly ranked or identified [42].

The following labels, which have been suggested for the evaluation a classification model based on the area under a ROC curve [43], will be used in this thesis as one description of the classifiers:

- 0.50 to 0.75 = fair
- 0.75 to 0.92 = good
- 0.92 to 0.97 = very good
- 0.97 to 1.00 = excellent

Although the area under the curve will be considered in this study as a guide to the performance of the descriptors, it is not a guaranteed answer. It is possible for a curve with a higher AUC to perform worse within a specific region of the ROC space, so classifier evaluation must consider the desired target sensitivity levels as well as error costs. Classifier thresholds which produce points on the left-hand side of the ROC space are “conservative” in that they will classify an instance as positive only with strong evidence so there will be very few false positive errors. In the upper right area of ROC space, classifiers can be considered more “liberal” since they will make a positive classification on weaker evidence. This means that they may be able to identify close to all positive instances correctly at the expense of a high false positive rate [40]. To set the appropriate threshold value for a decision threshold, knowledge of the error costs and the prevalence of the disease must be considered.

4.3 Accuracy

Evaluating the accuracy of a descriptor can provide additional insight into selecting a decision threshold value [44]. The accuracy of a descriptor is based on the percentage of correct classifications in the study:

$$accuracy = \frac{true\ positives + true\ negatives}{positives + negatives} \quad [40].$$

The accuracy of each descriptor is evaluated and graphed to illustrate the variation based on the threshold value and the point of maximum accuracy is shown on the ROC curve graphs for each descriptor.

4.4 Regression Models

A linear regression model is not appropriate for this project. Since the dependent variable can be expressed by the categorical values zero and one, the assumption of common variance in linear regression is not valid. In addition, a linear model could predict values of the dependent variable that were less than zero or greater than one. Since linear regression models do not apply, logistic regression models were fit for each of the static descriptors and for combinations of the descriptors to evaluate the potential benefit of using multiple descriptors [45] [46].

The first step in defining a logistic regression model is to encode the dependent variable. In this case a variable, π , is defined as the ratio of images classified as plaque at a descriptor threshold value to total plaque images, where $0 \leq \pi \leq 1$. Next, a threshold odds ratio, $\pi/(1 - \pi)$, is computed. This ratio varies from zero to positive infinity. The transformation from the odds ratio to the log odds, also called the logit function, maps the values from negative infinity to positive infinity. It also has the symmetric property that the log odds of being plaque are the opposite of the log odds of being non-plaque [46]:

$$\log_e \left(\frac{\pi}{1 - \pi} \right) = -\log_e \left(\frac{1 - \pi}{\pi} \right)$$

The logistic regression for a single descriptor is:

$$\log_e \left(\frac{\pi}{1 - \pi} \right) = \alpha + \beta x$$

or more generally for the multiple logistic regression:

$$\log_e \left(\frac{\pi}{1 - \pi} \right) = \alpha + \beta_1 x_1 + \beta_2 x_2 + \dots$$

In this thesis, the model parameters were fit using the maximum likelihood loss function which maximizes the conditional probability of the data given the model parameters [45] [47]. An example graph for the circularity descriptor model is shown in Figure 25.

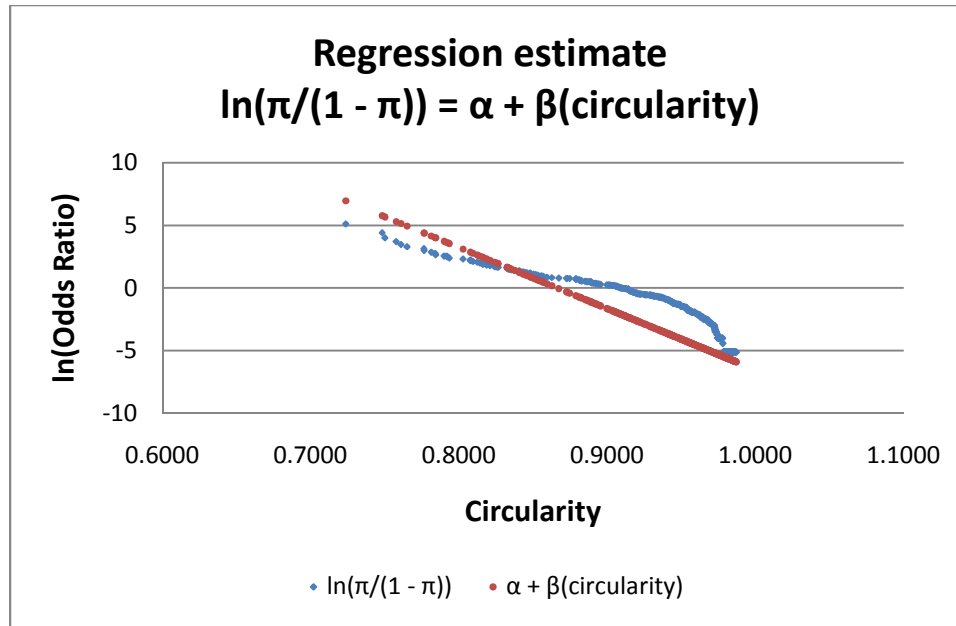


Figure 25: The log odds compared to the regression estimate based on the circularity descriptor.

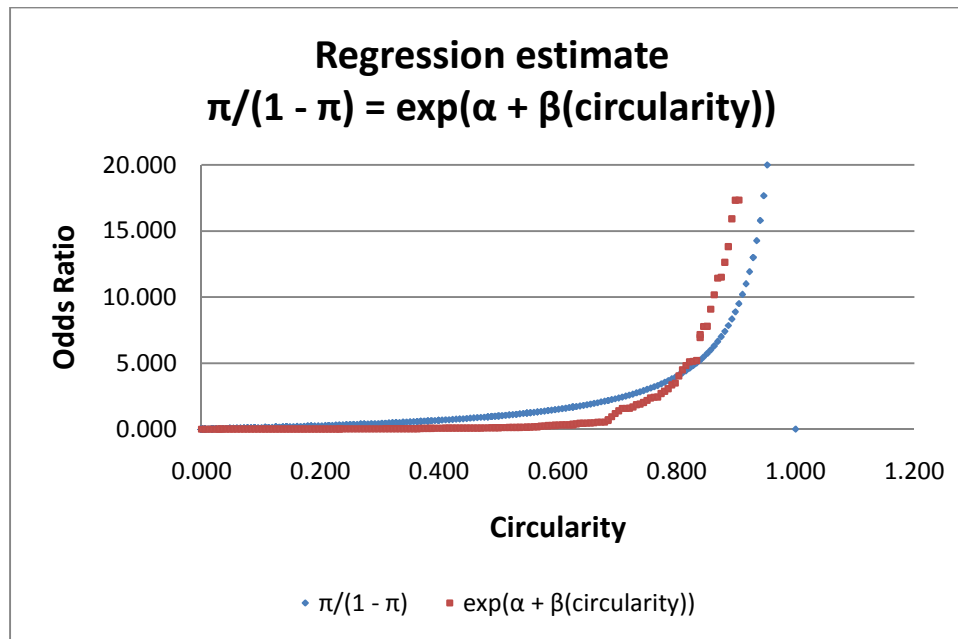


Figure 26: Exponentiation of the log odds to yield the odds ratio at each level.

The p-value for each descriptor is used to test for evidence of a relationship between the predictor and the response variable. The null hypothesis asserts that there is no change in the odds ratio based on the predictor variable. The estimated coefficient of an

independent variable is the estimated change in the log odds for each unit change in the predictor, so exponentiation estimates the odds ratio at each threshold level as shown in Figure 26. An estimated coefficient of zero yields an odds ratio of one; and therefore, it implies that the probability of “plaque” is equal to the probability of “not plaque” so that the variable has no effect [45].

Solving to estimate the probability π , the ratio of plaque images classified at a descriptor threshold value to total plaque images, yields:

$$\pi = \frac{\exp(\alpha + \beta(\text{circularity}))}{1 + \exp(\alpha + \beta(\text{circularity}))}$$

which is shown in Figure 27.

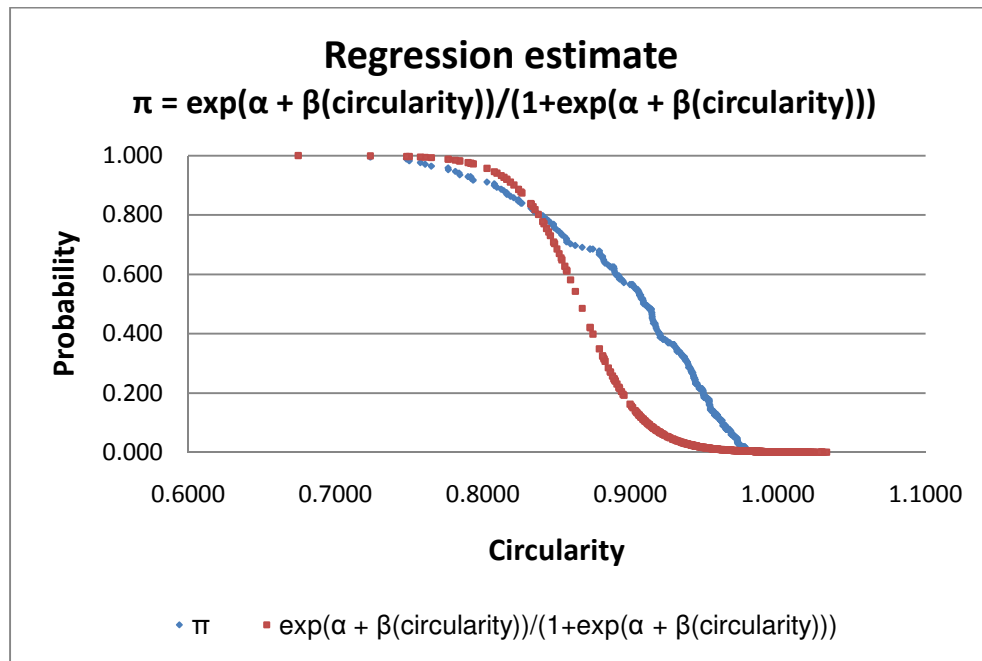


Figure 27: The probability of plaque estimated based on the circularity descriptor.

In addition to the logistic regression model parameters, Minitab was used to produce a table of measures of association between the response variable and predicted probabilities. The tabulation of concordant and discordant pairs examines the

relationship between each possible pair of plaque and non-plaque slices and indicates whether the image slice with the plaque has a higher predicted probability of plaque. The percentage of concordant pairs is equivalent to the area under the ROC curve [45] which measures the probability that in a random pair consisting of a normal and an abnormal image, the descriptor will allow them to be correctly ranked or identified [42].

The Goodman-Kruskal gamma further evaluates the association between the variables by calculating the difference between the probability of getting a concordant pair and that of getting a discordant pair:

$$\gamma = \frac{P(\text{concordant}) - P(\text{discordant})}{P(\text{concordant}) + P(\text{discordant})}$$

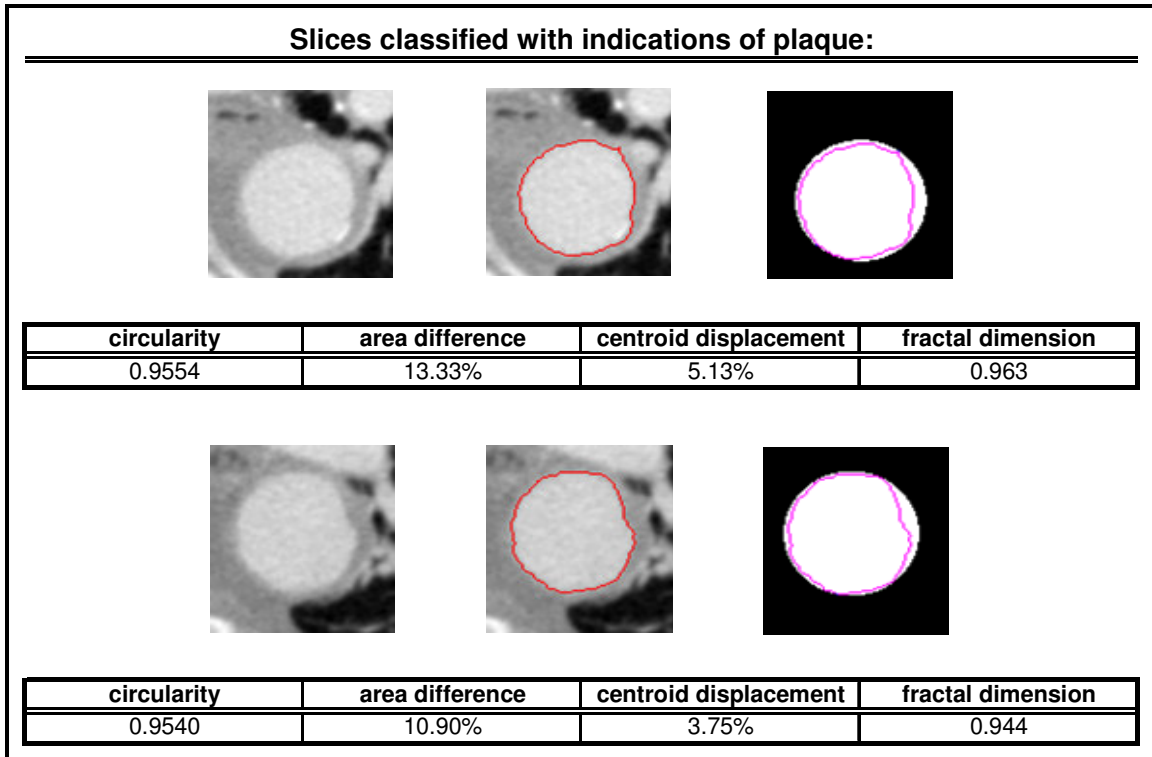


Figure 28: Samples and descriptor values for images slices classified with indications of plaque.

4.5 Slice Classification Examples

As stated earlier, the reported results are based on images for which two experts made identical determinations on the presence or absence of visible plaque indications. This section illustrates examples of slice classifications and the outer border of the lumen region calculated using this defined methodology.

Figure 28 displays two images assessed as having indications of plaque, and Figure 29 shows two image samples classified as normal. The leftmost image is the original CT image which the experts evaluated. The second image shows the computed perimeter outline superimposed on the original image. In the third frame, the estimated perimeter of the lumen is shown in red, and the smallest enclosing circle is highlighted in white. The calculated descriptors for the image slices are shown in the figures for comparison.

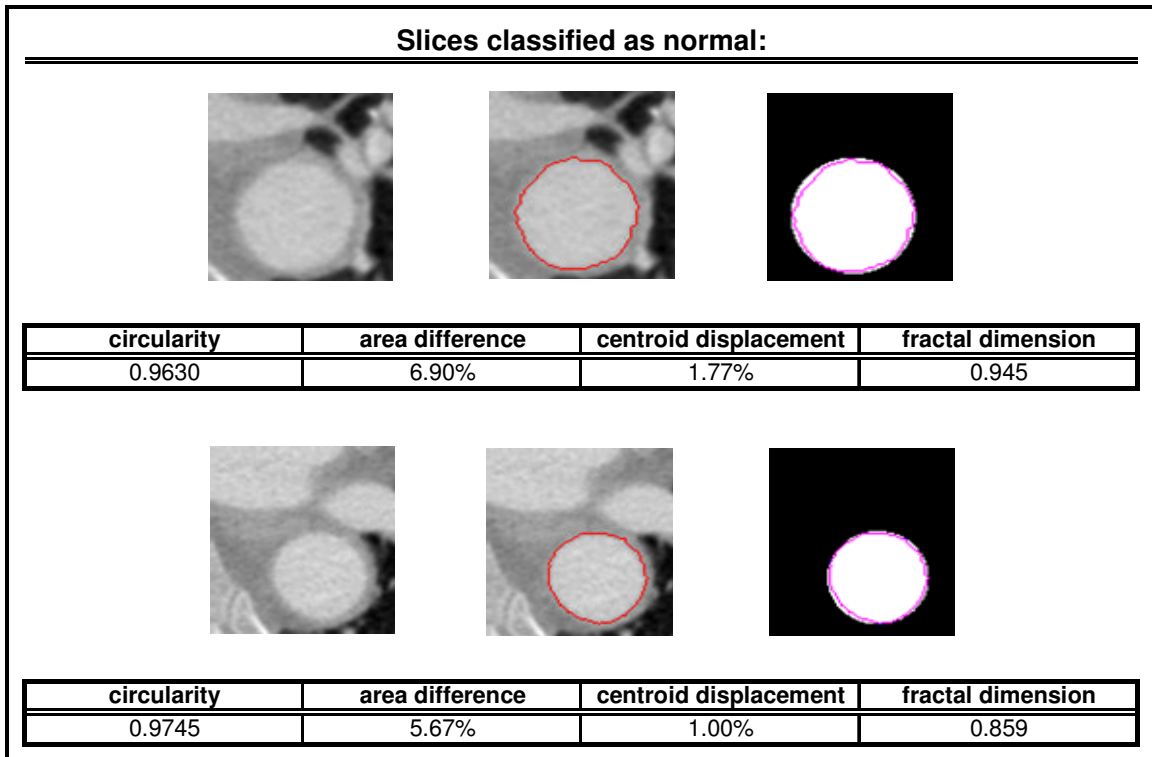


Figure 29: Samples and descriptor values for image slices classified as having no visible indications of plaque.

In addition, there was a small group of slices that the experts declined to classify based on their visual inspection. Examples of these slices are illustrated in Figure 30 and were not included in the classification statistics for the study.

In some image slices, there were vessel branches or other structures which had HU values similar to that of the lumen. In these cases, the resulting binary output regions were connected by one or more pixels which prevented the automated separation using the PCNN output. Figure 31 illustrates examples of these images and the perimeters and areas that were eliminated from consideration because of this problem.

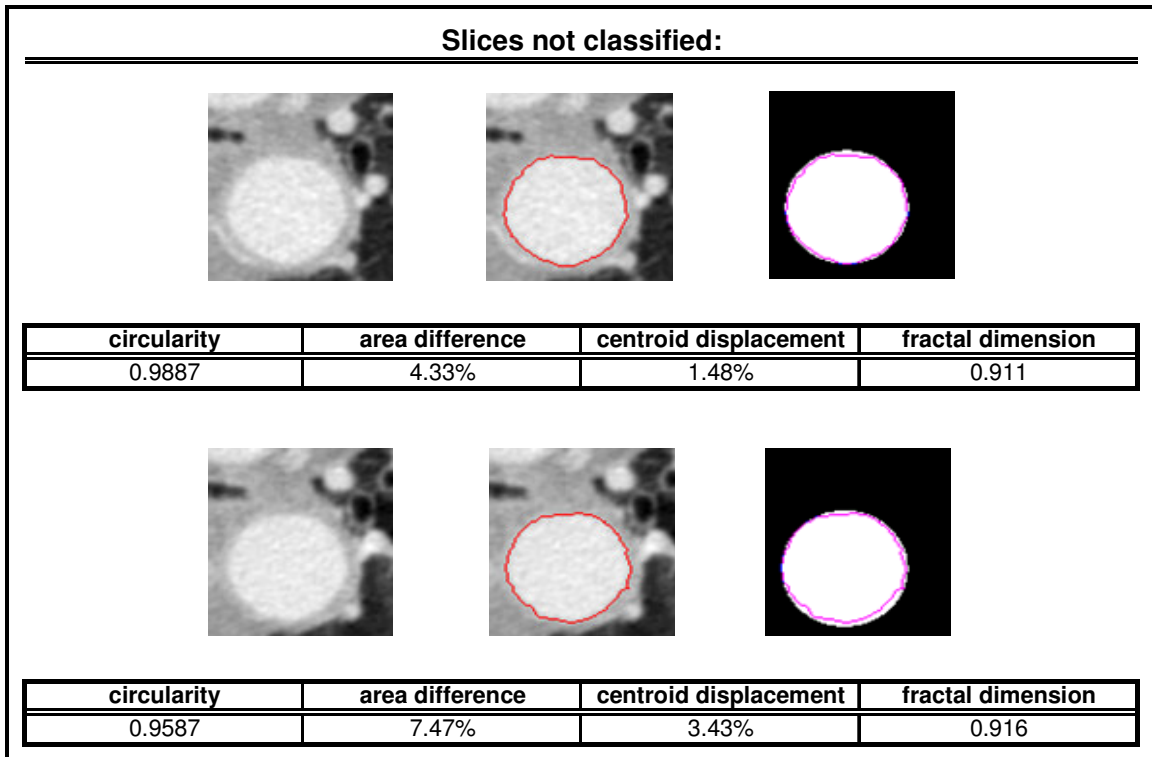


Figure 30: Samples and descriptor values for image slices not classified.

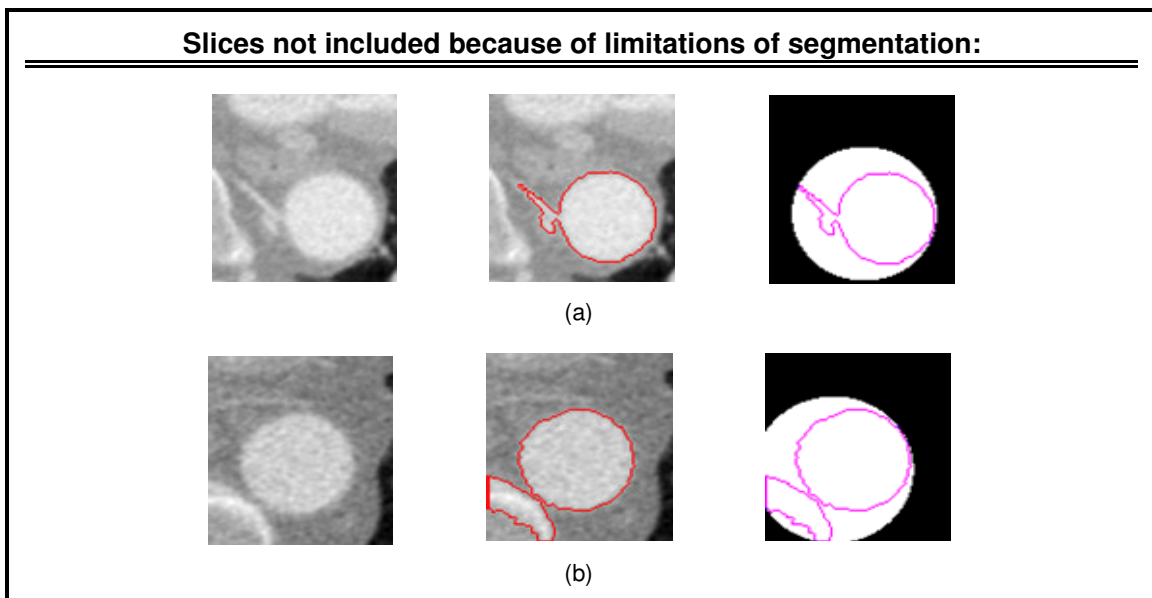


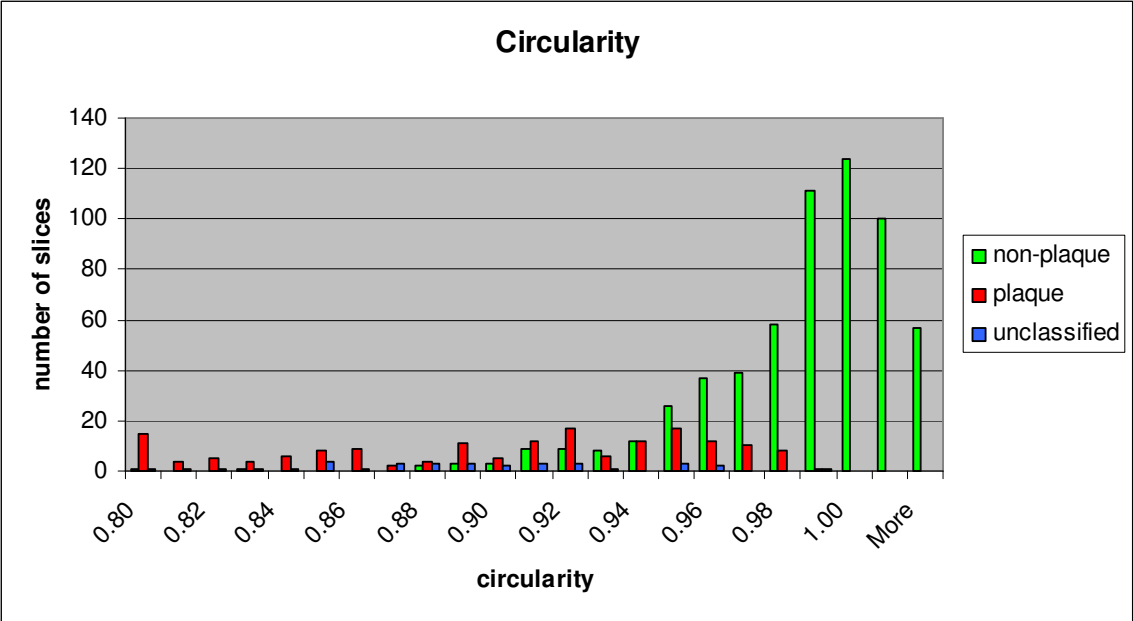
Figure 31: Samples of images slices in which a vessel branch (a) or another structure (b) prevents automated segmentation using the PCNN region output.

5. STATIC DESCRIPTOR RESULTS

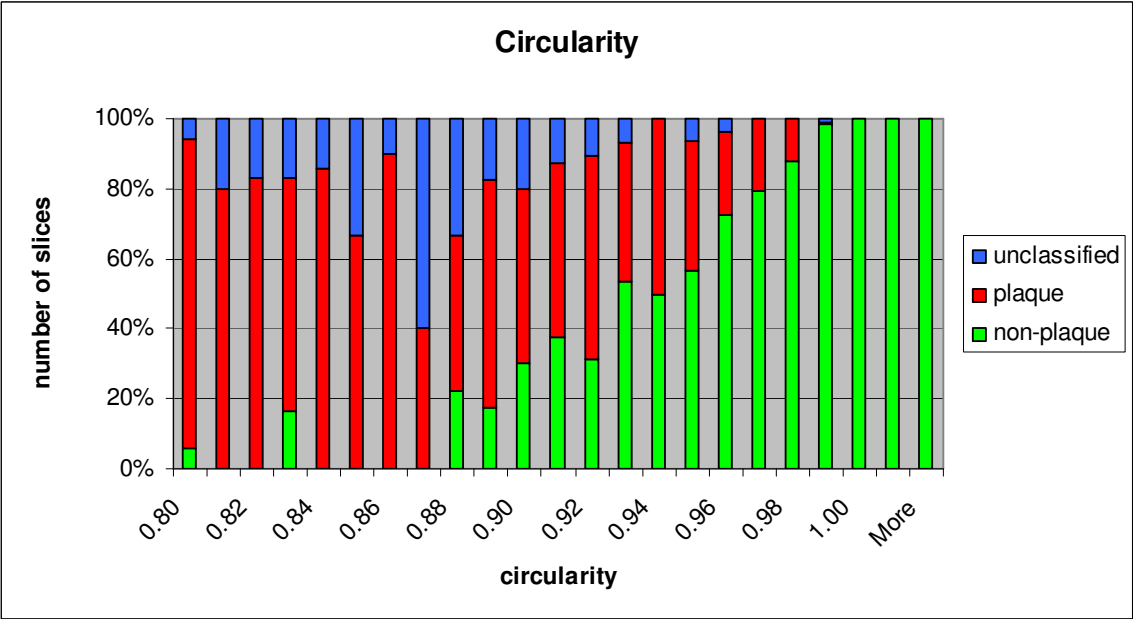
5.1 Circularity

The histograms in Figure 32 tabulate the values for the circularity of the lumen perimeter. Figure 32(a) displays the slice counts for each histogram interval for circularity values from the reference set. Figure 32(b) presents the classifications as a percentage of the total number of slices in each circularity interval. As hypothesized, the circularity values for slices which were not classified as having visible indications of plaque were, for the most part, closer to one although there is not an absolute separation.

The ROC curve for circularity is shown in Figure 33. The area under the ROC curve is 0.94 which is in the range rated as a very good classifier (0.92 to 0.97). At the point of the highest accuracy, shown at the yellow triangle, approximately 60% of the positive slices were classified correctly with a circularity descriptor threshold of .92. This threshold resulted in approximately 4% false positives. To reach 90% of the slices containing indications of plaque, the threshold would need to be increased to .96 at an associated cost of almost 20% false positive identification.



(a)



(b)

Figure 32: Circularity values for 802 image slices: 600 non-plaque, 168 plaque, and 34 unclassified.

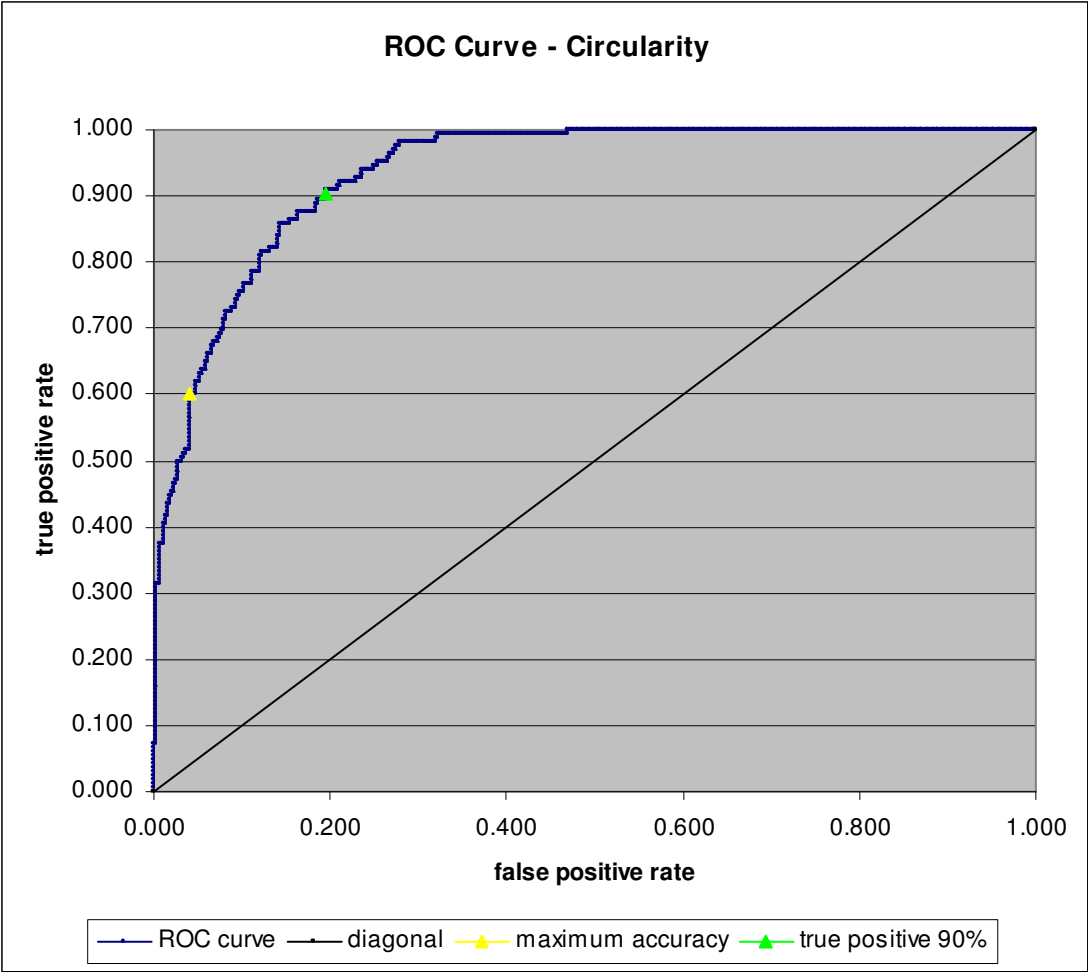
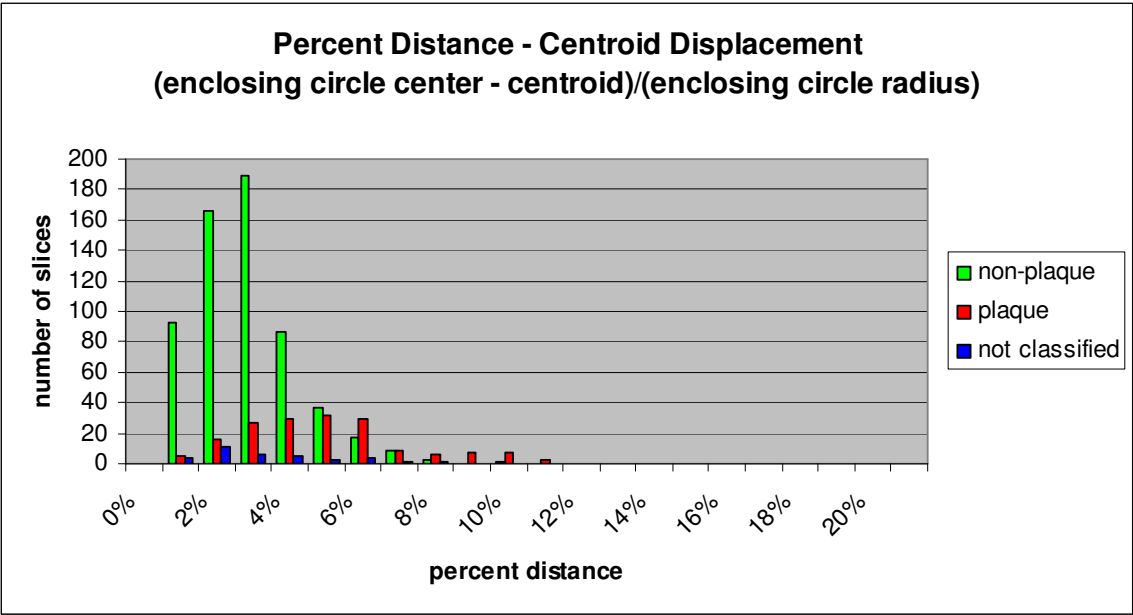


Figure 33: ROC curve for circularity.

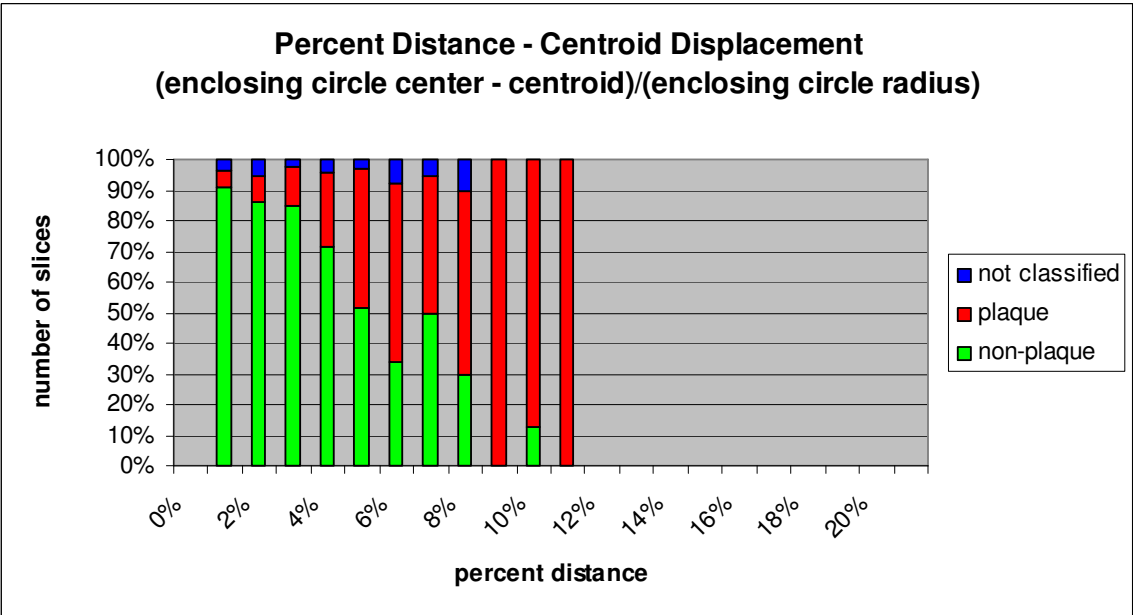
5.2 Centroid Displacement

The histograms in Figure 34 show the values for the percent difference between the best estimate of the center of the artery and the centroid of the lumen. Figure 34(a) displays the slice counts for each interval of centroid displacement values. Figure 34(b) shows the classifications for the reference set as percentage of the total slices for each range of values. As predicted, the displacement values for slices which had visible indications of plaque were higher.

The ROC curve for the centroid displacement is shown in Figure 35. The area under the curve is 0.77 which is at the low end of the range of 0.75 to 0.92, rated as a good classifier. While rated by the reference description [45] as good, at the point of the highest accuracy shown at the yellow triangle, only 43% of the positive slices were classified correctly by the descriptor using a threshold of 4.7%. At this threshold level, approximately 6% of the normal slices were classified as false positives. To reach the level of identifying 90% of the slices containing indications of plaque, the threshold would need to be changed to 1.9% with a significant increase in the associated cost of almost 60% false positive identification.



(a)



(b)

Figure 34: Percent difference values for the best estimate of the center of the artery and the centroid of the lumen for 802 image slices: 600 non-plaque, 168 plaque, and 34 unclassified.

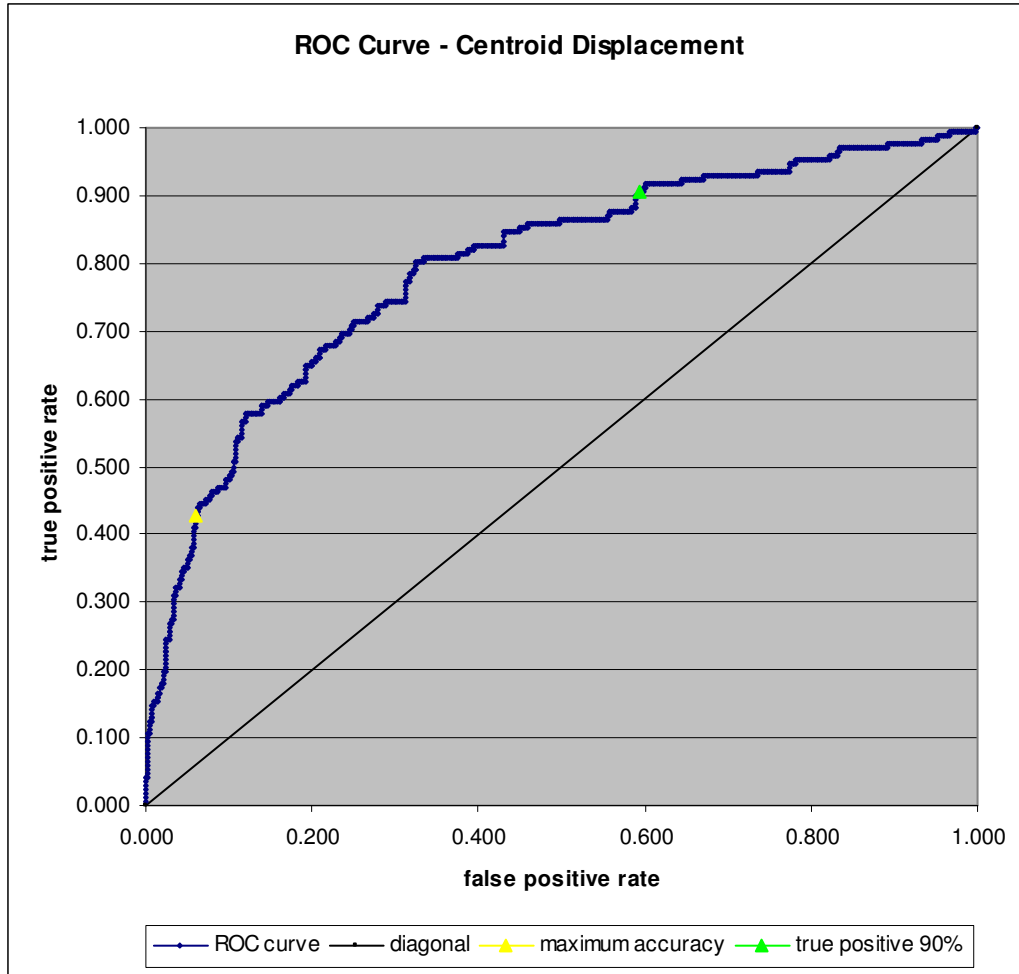
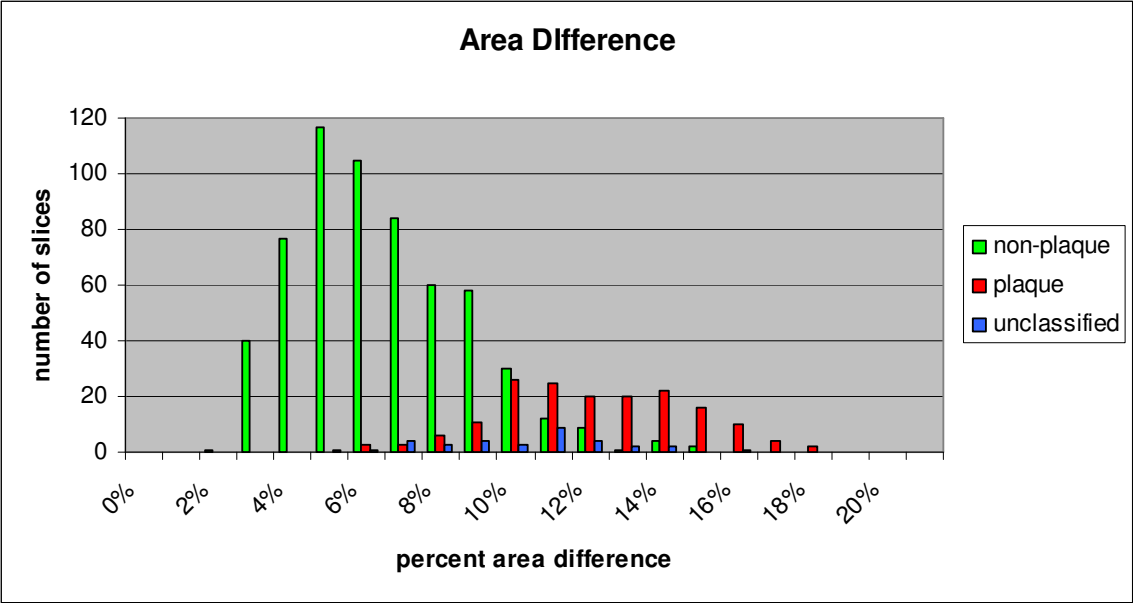


Figure 35: ROC curve for centroid displacement.

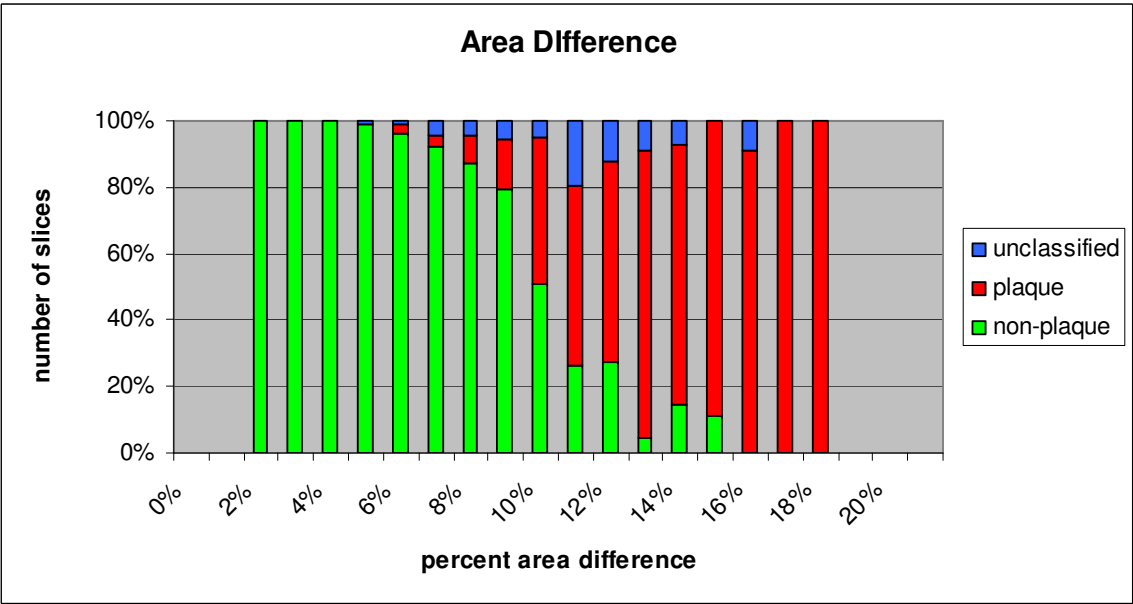
5.3 Area Difference

The histograms in Figure 36 show the percentage difference in area between the lumen and the smallest enclosing circle containing the lumen. Figure 36(a) displays the slice counts for the reference set in each interval of area difference values. Figure 36(b) displays the slice classifications as a percentage of the total slices in each interval. For the most part, the area difference values for slices with visible indications of plaque were higher reflecting the displacement of the lumen area.

The ROC curve for the area difference is shown in Figure 37. The area under the curve is 0.96 which is in the range of 0.92 to 0.97 rated as a very good classifier. At the point of the highest accuracy, shown at the yellow triangle, approximately 83% of the positive slices were classified correctly by the descriptor using a threshold of 9.4%. At this threshold level, between 7% and 8% of the normal slices were classified as false positives. To reach the level of identifying 90% of the slices containing indications of plaque, the threshold would need to be changed to 8.4% with a corresponding increase to almost 15% false positive identification.



(a)



(b)

Figure 36: Percent difference in area between the lumen and the smallest enclosing circle containing the lumen for 768 image slices: 600 non-plaque, 168 plaque, and 34 unclassified.

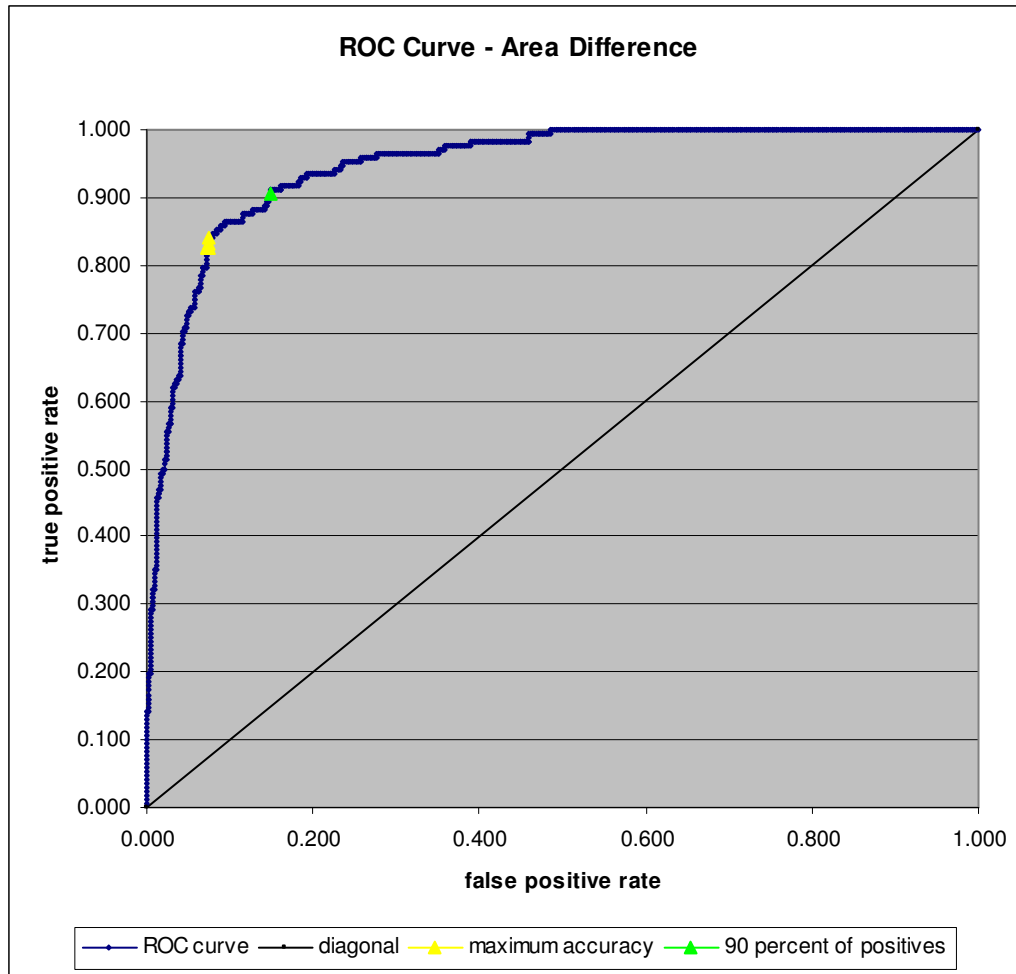
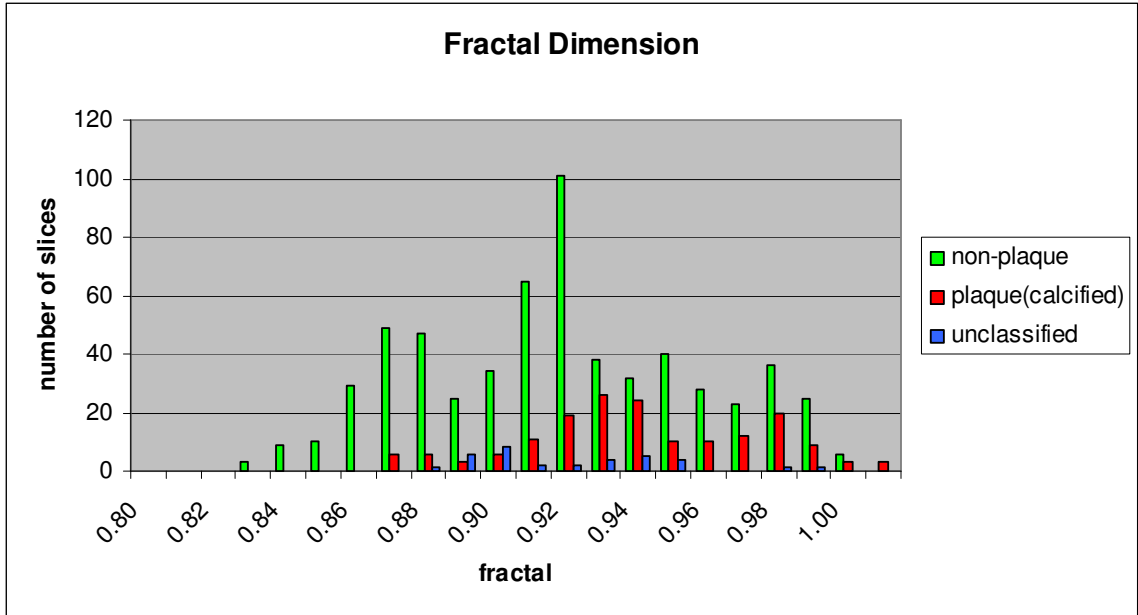


Figure 37: ROC curve for area difference.

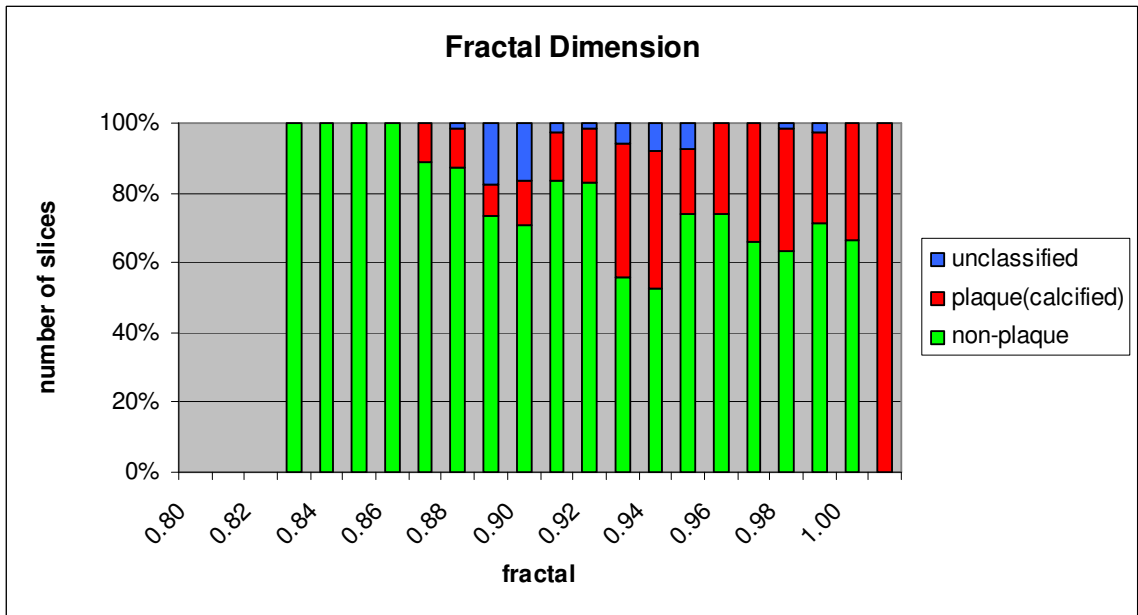
5.4 Fractal Dimension

The histograms in Figure 38 show the fractal dimension of the perimeter of the lumen. The values for slices which did not have visible plaque indications were generally lower which would be a sign of a less complex surface perimeter. Figure 38(a) shows the slice counts for each interval of the fractal dimension values. Figure 38(b) illustrates the slice classifications for the reference set as a percentage of the total slices in each range of values.

The ROC curve for fractal dimension is shown in Figure 39. The area under the curve is 0.67 which is in the range of 0.50 to 0.75 rated as only a fair classifier. The point of the highest accuracy of the fractal dimension classifier was 79%, shown at the yellow triangle. This point would not be considered a reasonable classification since only 2% to 3% of the true positives were identified at this threshold. To reach the level of identifying 90% of the slices containing indications of plaque, the associated cost rises to over 70% false positive identification. To reach even a 75% true positive rate, the false positive rate is over 40%.



(a)



(b)

Figure 38: Fractal dimension of the lumen perimeter for 802 image slices: 600 non-plaque, 168 plaque, and 34 unclassified.

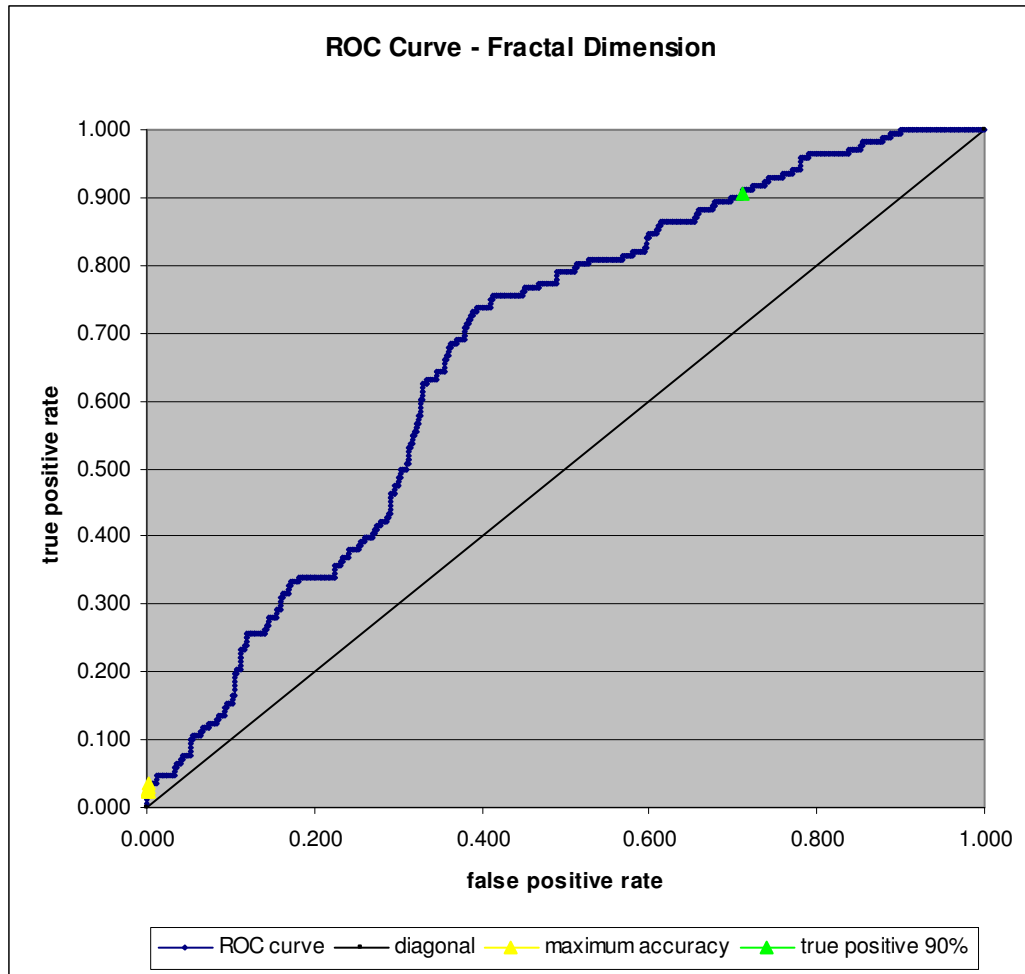


Figure 39: ROC curve for fractal dimension.

5.5 Comparison of the Static Descriptors

All of the descriptors have some merit in adding information about the classification of the slices. Figure 40 shows the ROC curves for the static descriptors plotted on the same graph. Table 4 summarizes the area of the ROC space under each classifier curve. Of particular note is the area difference between the lumen and the smallest enclosing circle that contains all of the perimeter points of the lumen region. This descriptor was able to best discriminate the slices in agreement with the gold standard classification of plaque or no plaque indications. The area difference descriptor was less sensitive to image noise at the lumen edges, a more noticeable factor in the calculation of circularity and fractal dimension.

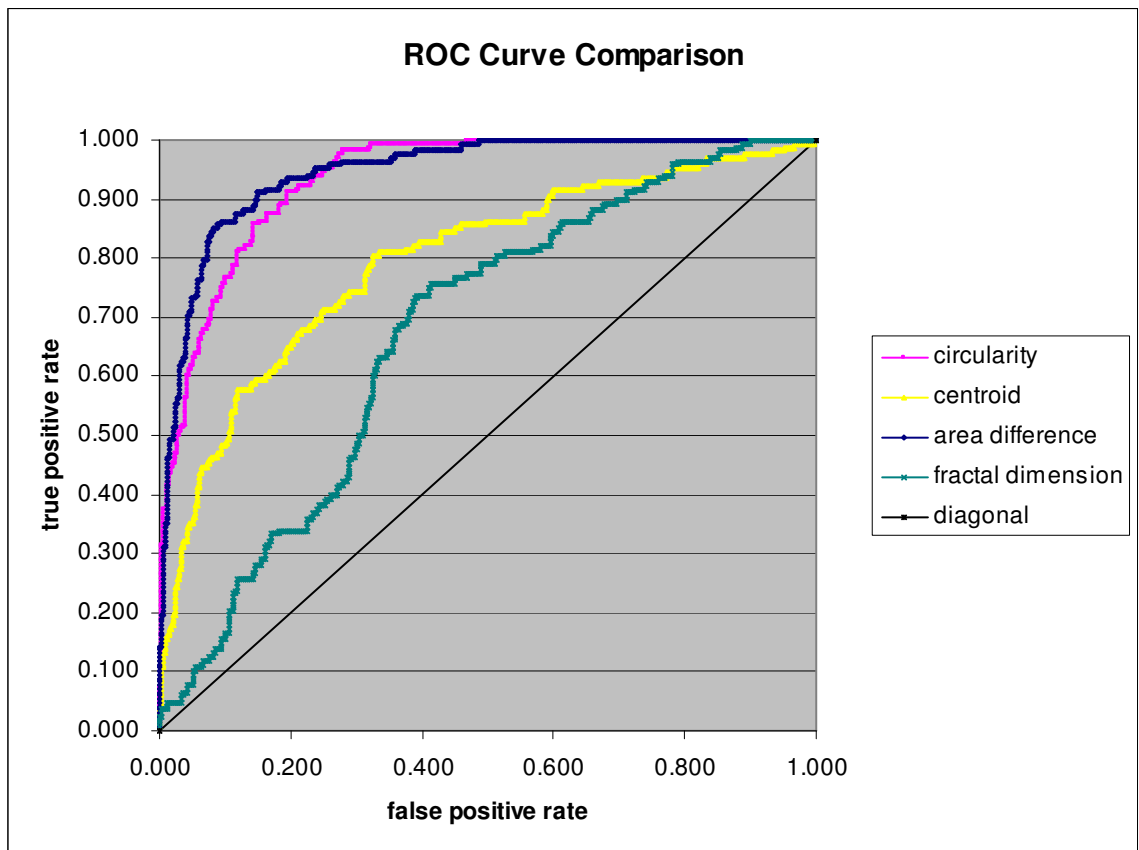


Figure 40: ROC Curves for all static descriptors.

Table 4: Classifier Comparison by Area under ROC Curve

Descriptor	Area Under Curve (AUC)	SE(AUC)	Classifier Rating
Circularity	0.94	0.01	0.92 to 0.97 = very good
Centroid Displacement	0.80	0.02	0.75 to 0.92 = good
Area Difference	0.96	0.01	0.92 to 0.97 = very good
Fractal Dimension	0.67	0.02	0.75 to 0.92 = good

5.7 Accuracy of the Static Descriptors

A further comparison of the descriptors is shown in Table 5 with the maximum accuracy level that they were able to achieve. Table 5 also breaks down the maximum accuracy figure to reflect both the numbers of true positives and true negatives that the descriptors could classify.

Again, the area difference was the strongest performer. As shown in Table 5, the maximum accuracy for the area difference descriptor is .91 which occurs for a threshold of 9.4%. At this threshold 141 of 168 true positive (plaque) images are classified as well as 555 of 600 true negative (non-plaque) image classifications. Figure 41 through Figure 44 illustrate how the accuracy values vary as the thresholds are adjusted for each descriptor.

Table 5: Accuracy Comparison

Descriptor	Maximum Accuracy	# True Positives	# True Negatives	TP + TN
Circularity	0.88	101	575	676
Centroid Displacement	0.83	72	564	636
Area Difference	0.91	141	555	696
Fractal Dimension	0.79	6	598	604

note: 768 total cases

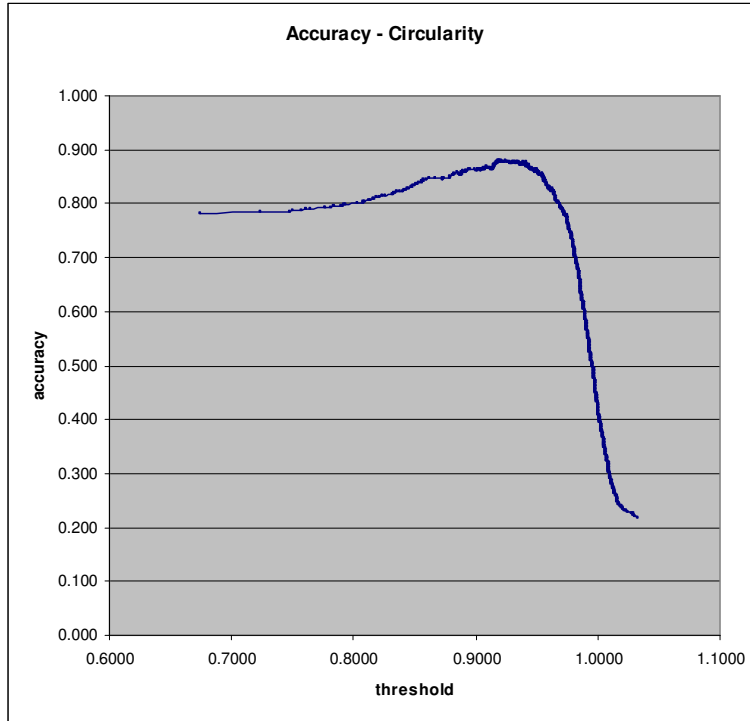


Figure 41: Accuracy of the circularity descriptor as the threshold varies.

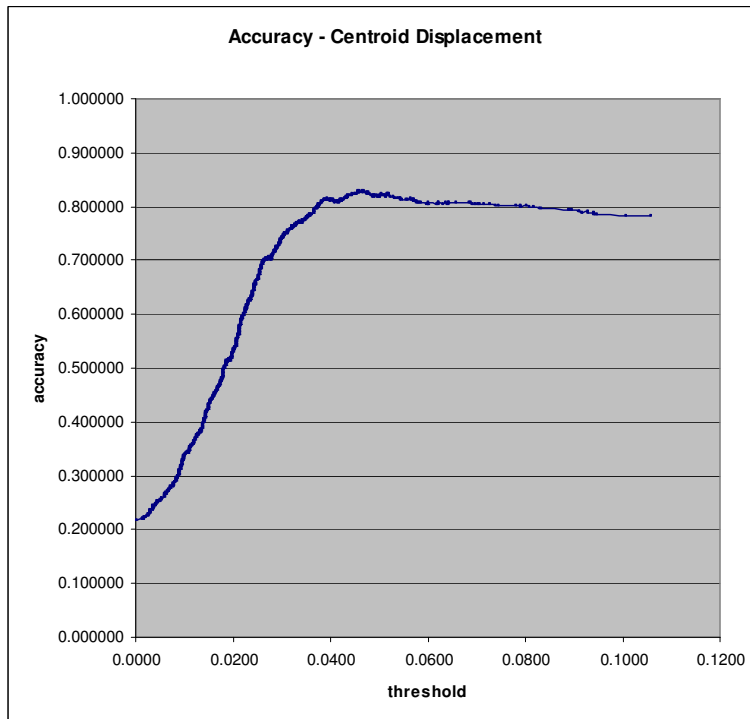


Figure 42: Accuracy of the centroid displacement descriptor as the threshold varies.

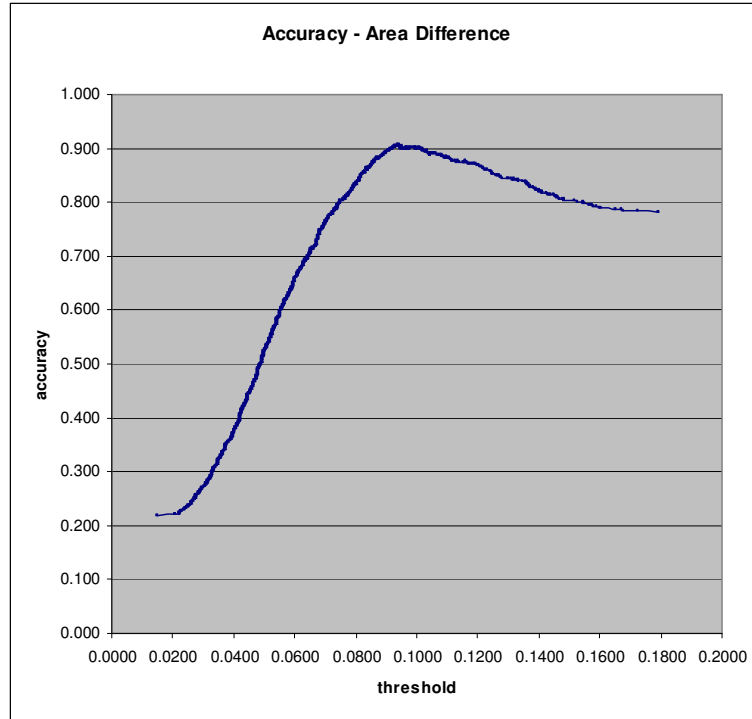


Figure 43: Accuracy of the area difference descriptor as the threshold varies.

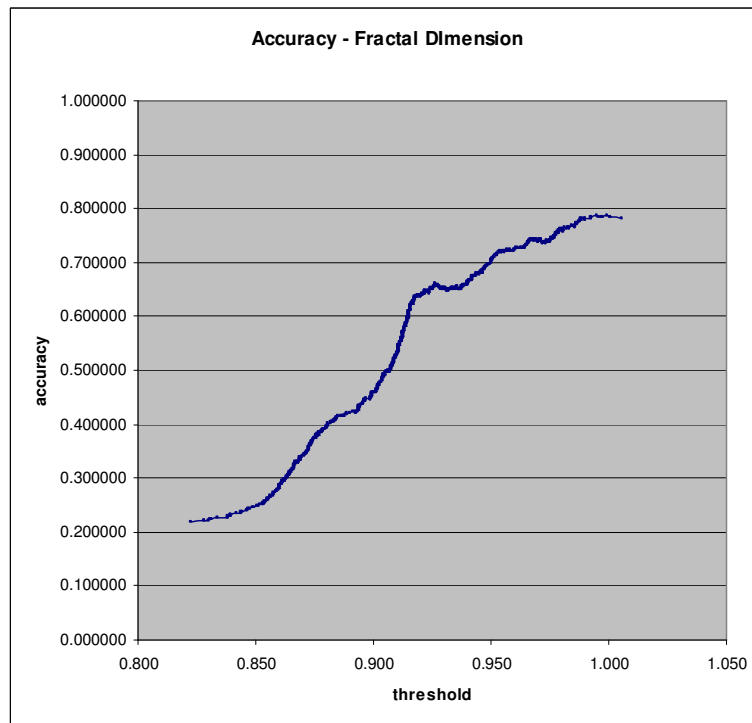


Figure 44: Accuracy of the fractal dimension descriptor as the threshold varies.

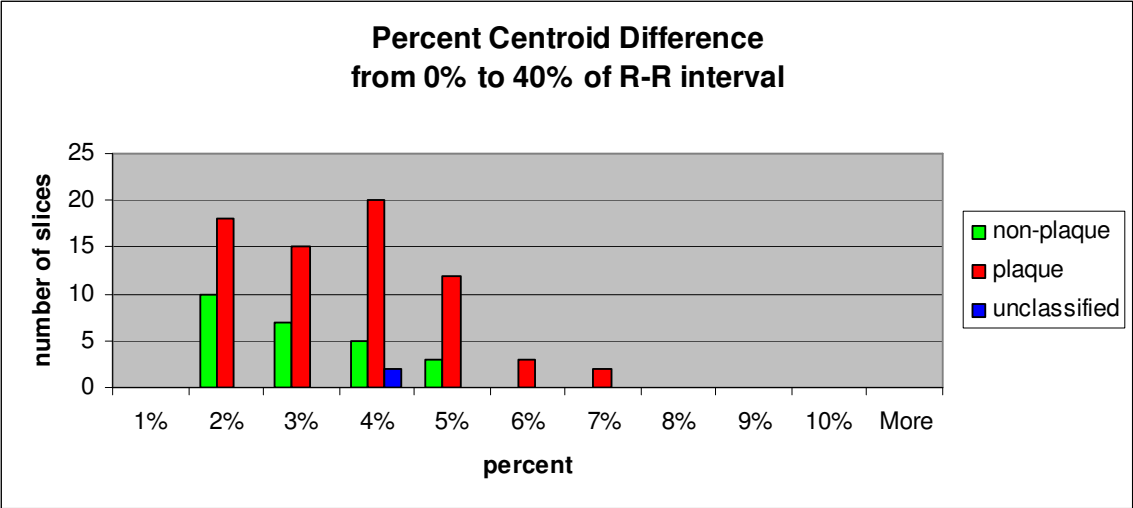
6. DYNAMIC DESCRIPTOR RESULTS

The time series results discussed below measure differences observed between slices acquired at the 0% and 40% increments in the R-R interval of the cardiac cycle. Only one of the eight studies considered for the static descriptors had the data available for the time series analysis. These preliminary results are based on a much smaller number of image slices from one patient.

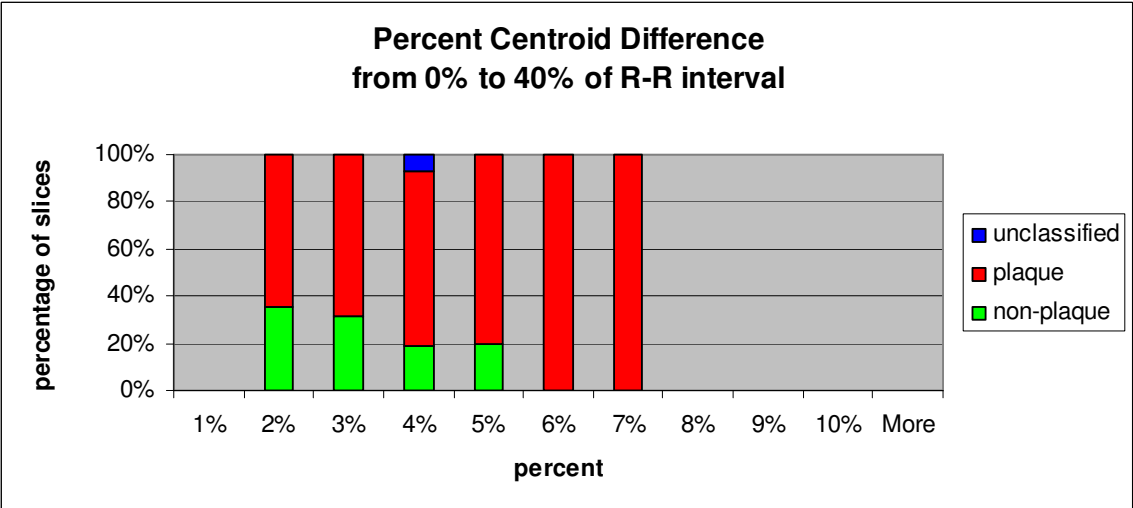
6.1 Centroid Dispersion

The centroid dispersion values are shown in the histograms in Figure 45. The difference in the centroid values in slices acquired at 0% and 40% increments in the R-R interval is calculated as a measure of asymmetry in aortic expansion. Figure 45(a) displays the slice counts in each interval for the reference set. Figure 45(b) presents the classifications as a percentage of the total number of slices in each interval.

The ROC curve for the centroid difference is shown in Figure 46. The area under the curve is 0.61 which is in the lower part of the range of 0.50 to 0.75 rated as a fair classifier. If the threshold is set lower than approximately 2%, the level at which 75% of the true positives are identified, the curve for the centroid difference descriptor falls below the diagonal line indicating a performance worse than random chance.



(a)



(b)

Figure 45: Percentage change in the position of the lumen centroid at 0% to 40% of the R-R interval for 97 image slices: 25 non-plaque, 70 plaque, and 2 unclassified.

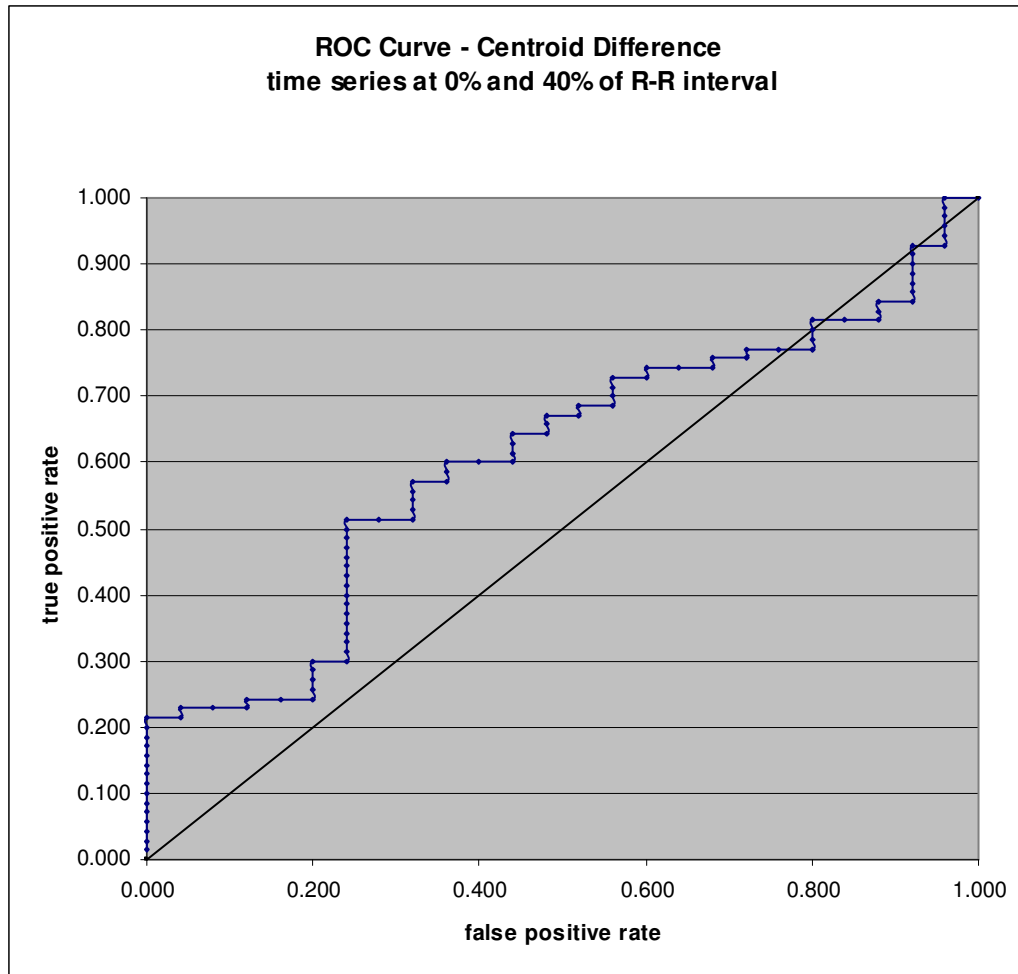
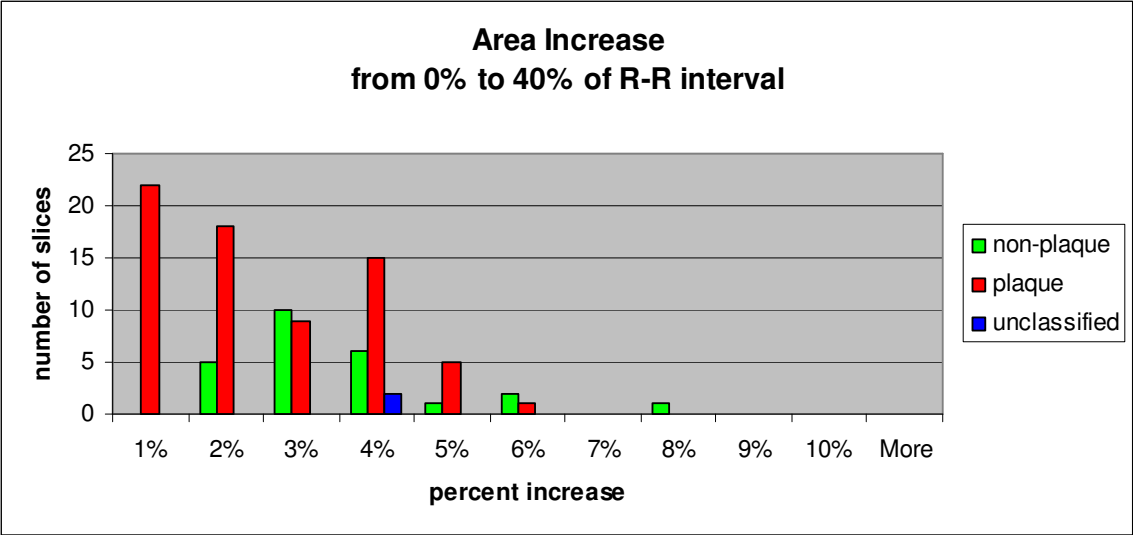


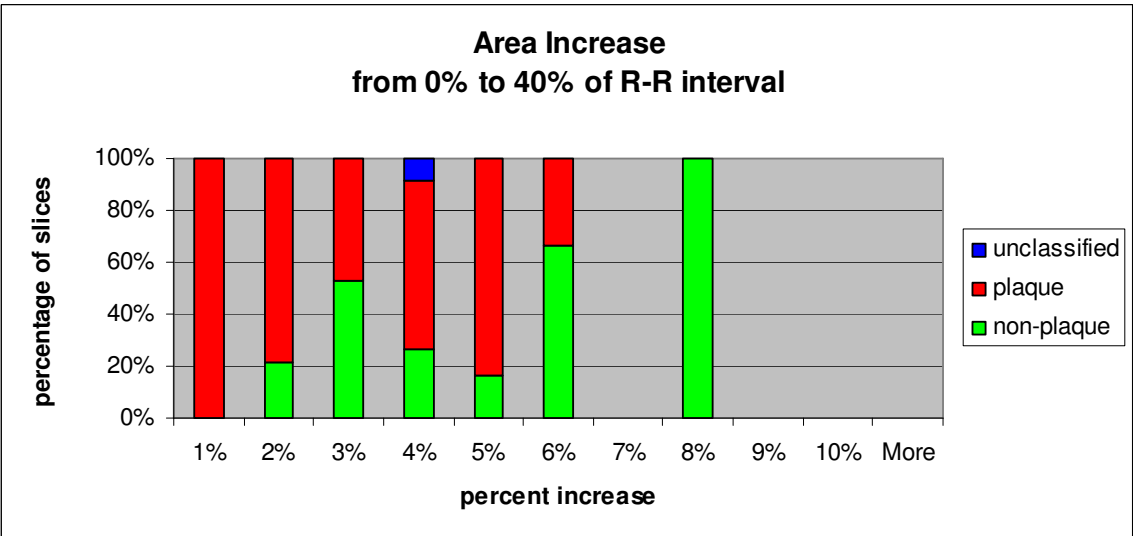
Figure 46: ROC Curve for centroid displacement.

6.2 Percentage Change in Lumen Area

The percentage change in the area of the lumen at 0% and 40% of the R-R interval in the cardiac cycle was calculated as an indication of vessel elasticity. The slice counts for each interval are shown in Figure 47(a) and the percentage of slices in each interval is shown in Figure 47(b). The ROC curve for the area difference is shown in Figure 48. The area under the curve is 0.68 which is in the range of 0.50 to 0.75 rated as a fair classifier.



(a)



(b)

Figure 47: Percentage change in the area of the lumen at 0% to 40% of the R-R interval for 97 image slices: 25 non-plaque, 70 plaque, and 2 unclassified.

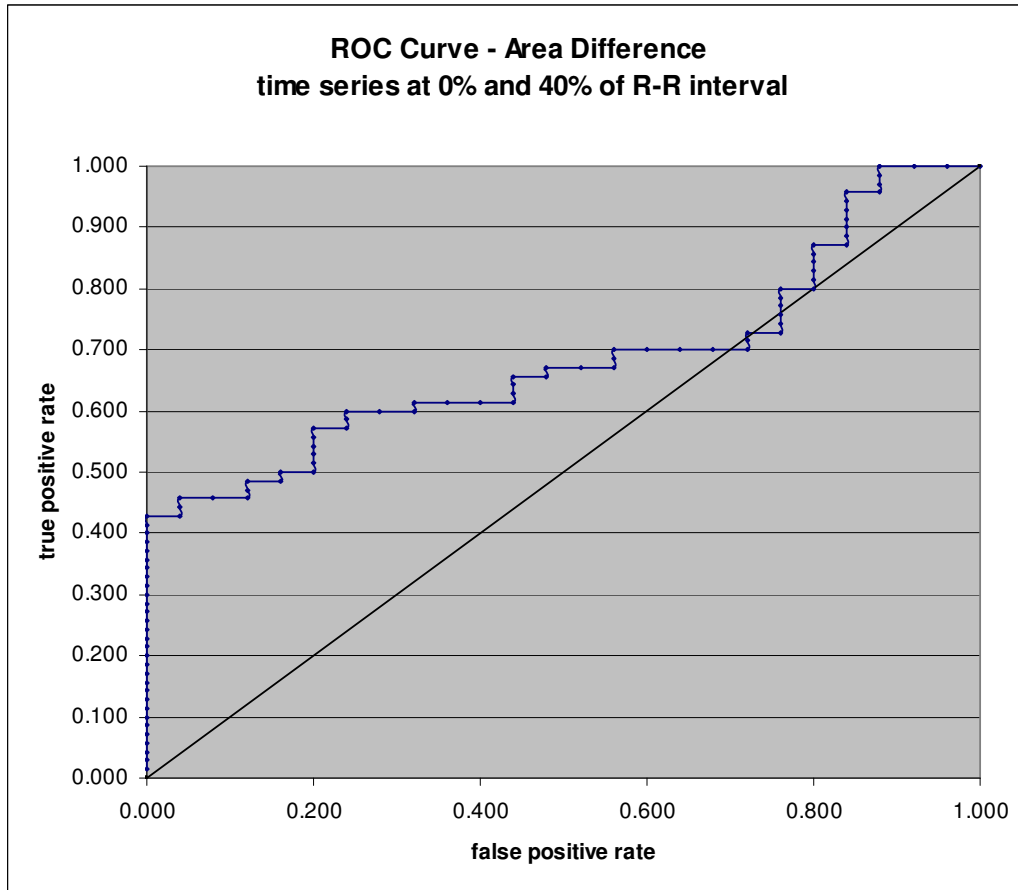


Figure 48: ROC Curve for area difference.

6.3 Comparison of the Time Series Descriptors

Figure 49 shows a comparison of the ROC curves for the time series descriptors. At 0.68, the area under the ROC curve for the area difference is greater than for the centroid displacement at 0.61; although based on the AUC value as shown in Table 6, both classifiers would be rated in the range of fair descriptors. Both descriptors have some merit in the classification of the slices. In comparing these classifiers, the cost of errors becomes an important factor because their relative performance reverses as the false positive rate increases. The limited amount of data available for this comparison limits the strength of any conclusion that would be drawn.

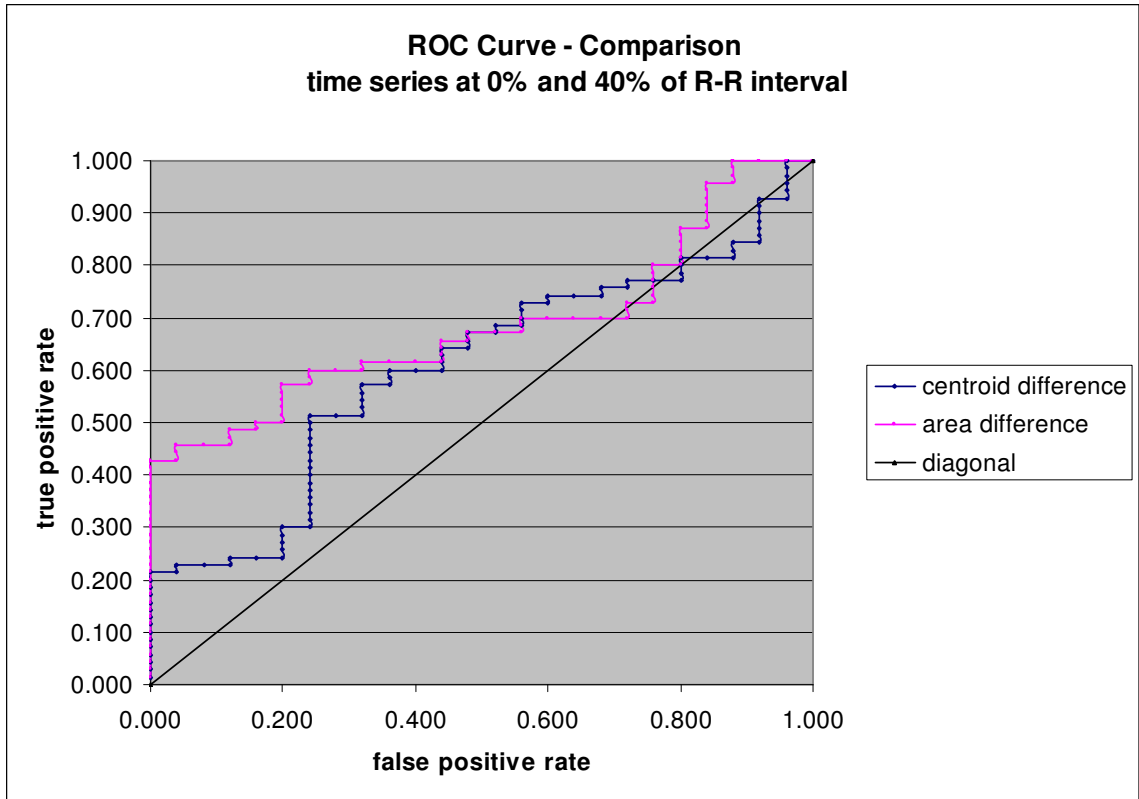


Figure 49: ROC Curves for time series descriptors.

Table 6: Classifier Comparison by Area under ROC Curve

Descriptor	Area Under Curve (AUC)	SE(AUC)	Classifier Rating
Centroid Difference	0.61	0.06	0.50 to 0.75 = fair
Area Difference	0.68	0.06	0.50 to 0.75 = fair

7. DISCUSSION

Since the area difference descriptor outperformed all of the other classification models, with an AUC of 0.96 which is considered to be in the “very good” [45] or “excellent” [41] rating category, this section will look more closely at the strengths and weaknesses of this descriptor.

The point on the ROC curve that corresponds to the maximum accuracy point is shown in yellow in Figure 50. That threshold of 9.4% identifies 84% of the true positive images with a cost of misclassifying 8% false positive images. As an example, if it was a requirement of this test to identify 90% of the positive images, the threshold could be moved to the point shown in green in Figure 50. The threshold which produces this point is approximately 8.4%. It identifies 152 (90%) true positive images at a cost of misclassifying 89 (15%) false positives.

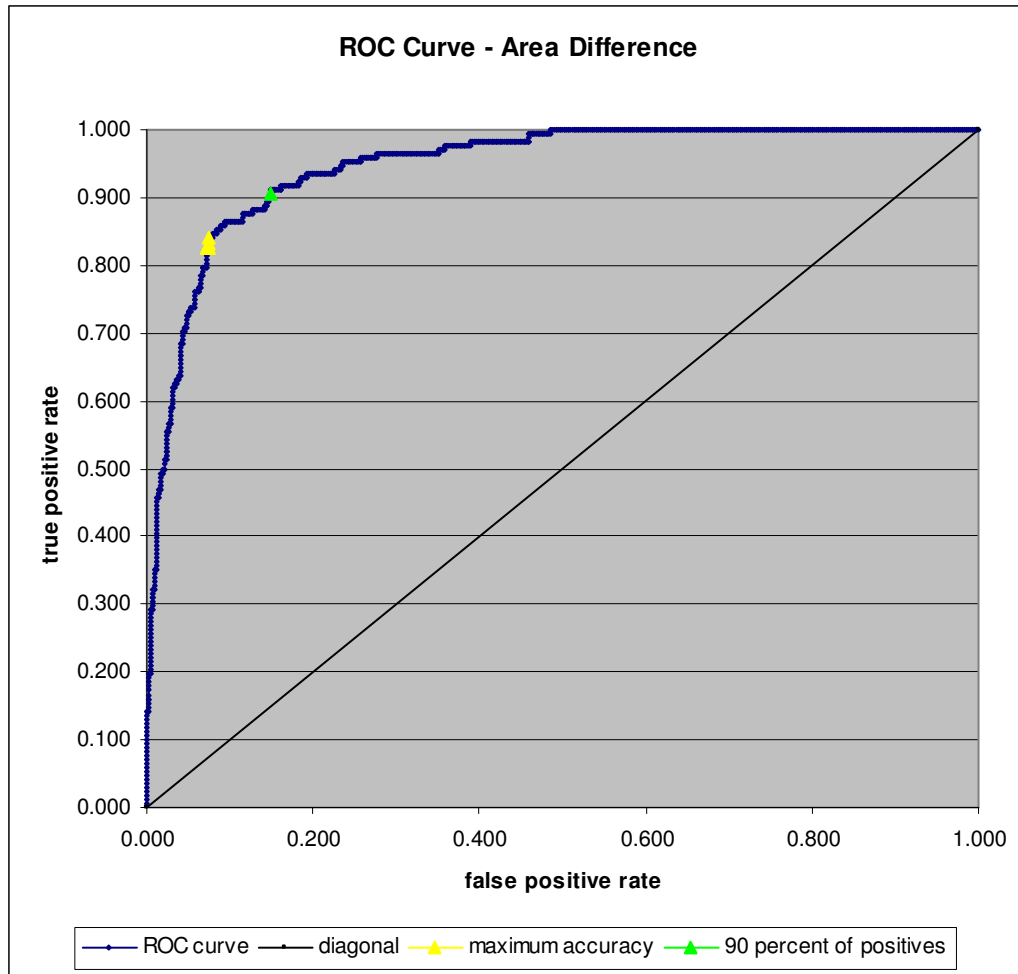


Figure 50: Accuracy measurements for the area difference descriptor.

7.1 Misclassification

At the threshold level that identifies 90% of the positive image slices, the 10% of images which are classified as false negatives by the area difference descriptor are highlighted in Figure 51. Figure 52 illustrates those false negatives which were below the 8.4% threshold for the area difference descriptor. Many of these slices contain an area visually identified as calcified plaque but which doesn't occlude a large area of the lumen. It can also be observed that the majority of these slices would have been correctly identified by the circularity descriptor at the threshold level which identified 90% of the positive slices.

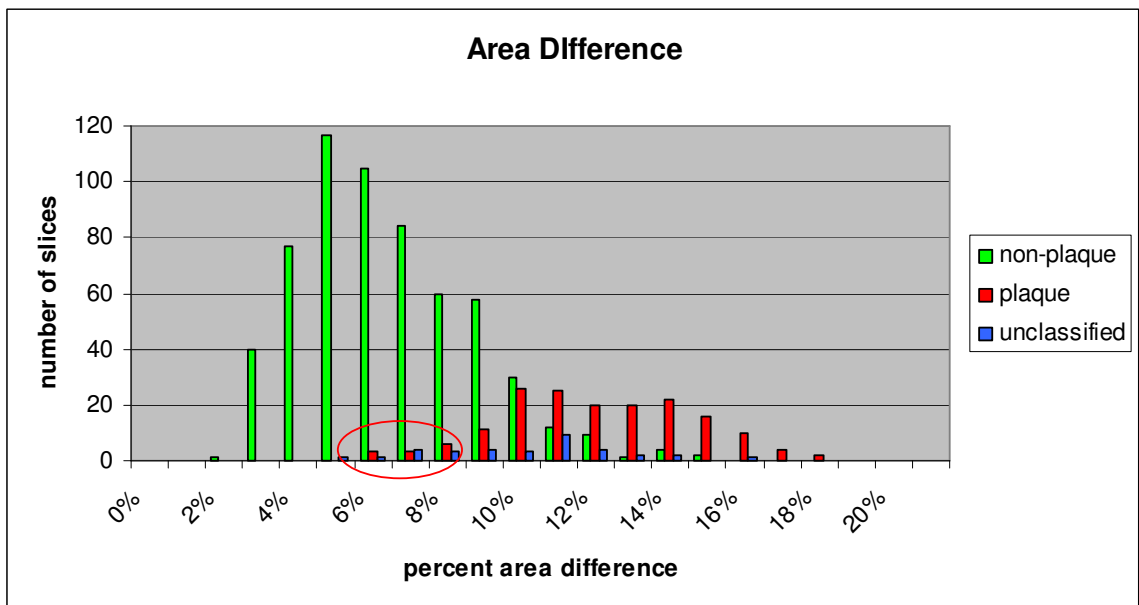
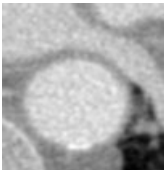
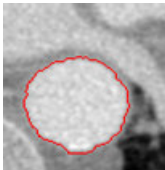

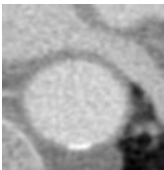
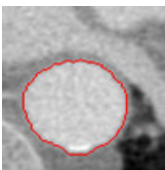

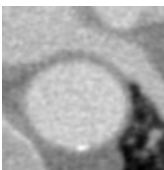
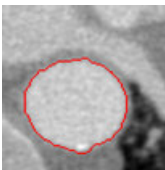

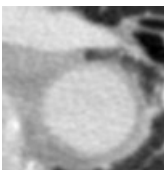
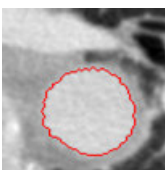

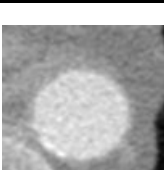
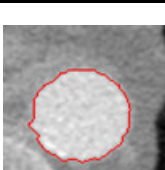

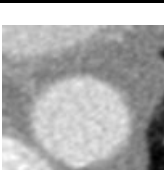
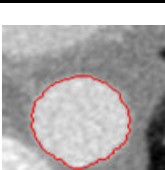

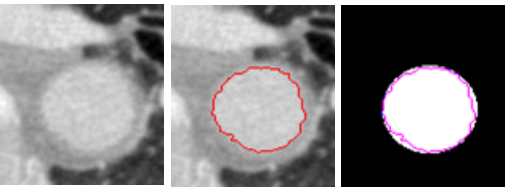
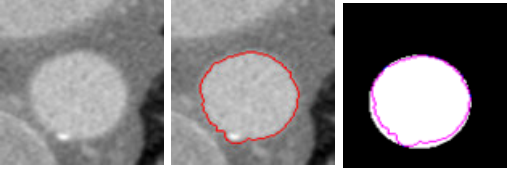
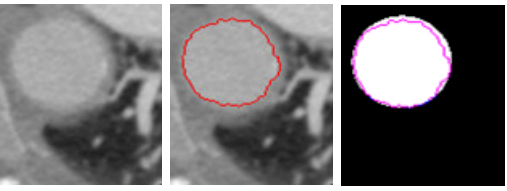
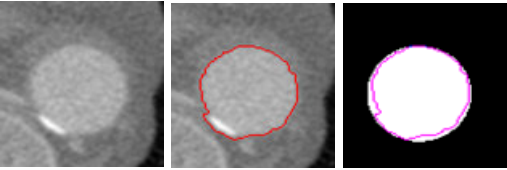
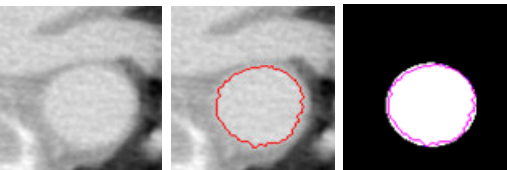
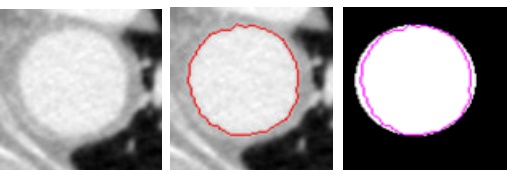


Figure 51: The red oval highlights the area of false negative slices.

slice identification	circularity	area difference	centroid displacement	fractal dimension
A3_P75_00010199.tif	0.9380	5.7%	1.3%	0.904
				
A3_P75_00010198.tif	0.9722	5.9%	3.2%	0.904
				
A3_P75_00010194.tif	0.9870	5.9%	1.9%	0.900
				
GJO_P75_00010110.tif	0.8955	6.3%	0.2%	0.967
				
A3_P75_00010100.tif	0.9493	6.6%	5.0%	0.930
				
A3_P75_00010128.tif	0.9438	6.7%	2.9%	0.980
				

(Continued on next page)

slice identification	circularity	area difference	centroid displacement	fractal dimension
GJO_P75_00010108.tif	0.9069	7.1%	0.6%	0.922
				
A3_P75_00010134.tif	0.9201	7.4%	4.2%	0.979
				
GJO_P75_00010219.tif	0.9147	7.6%	4.6%	0.932
				
A3_P75_00010096.tif	0.9300	7.6%	2.6%	0.980
				
KD_P75_00010148.tif	0.8788	7.7%	1.7%	0.969
				
A1_P75_00010173.tif	0.9537	8.0%	1.9%	0.943
				

(Continued on next page)

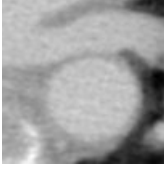
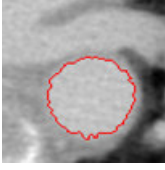

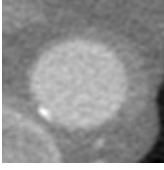
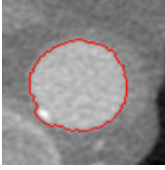

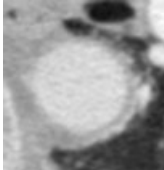
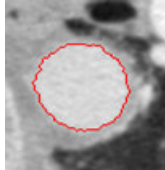

slice identification	circularity	area difference	centroid displacement	fractal dimension
KD_P75_00010149.tif	0.8323	8.0%	0.9%	0.970
				
A3_P75_00010087.tif	0.9168	8.1%	1.3%	0.901
				
GJO_P75_00010153.tif	0.9173	8.3%	2.7%	1.006
				

Figure 52: Image slices classified by physicians as having visual indications of plaque that would not be correctly classified by area difference descriptor.

At the opposite end of the ROC curve are the slices in the normal classification of the reference set which are identified as false positive by the area difference descriptor. These normal slices fall into the intervals highlighted by the green oval in the histogram in Figure 53. Figure 54 illustrates slices representative of the 15% of slices that would be identified as false positives. Several of these slices have an oval shape which might indicate in that area of the CT scan, the slices of the aorta did not meet the assumption that the slices would be orthogonal. Again in the case of these false positives, it is observed that many of these slices would have been correctly identified by the circularity descriptor.

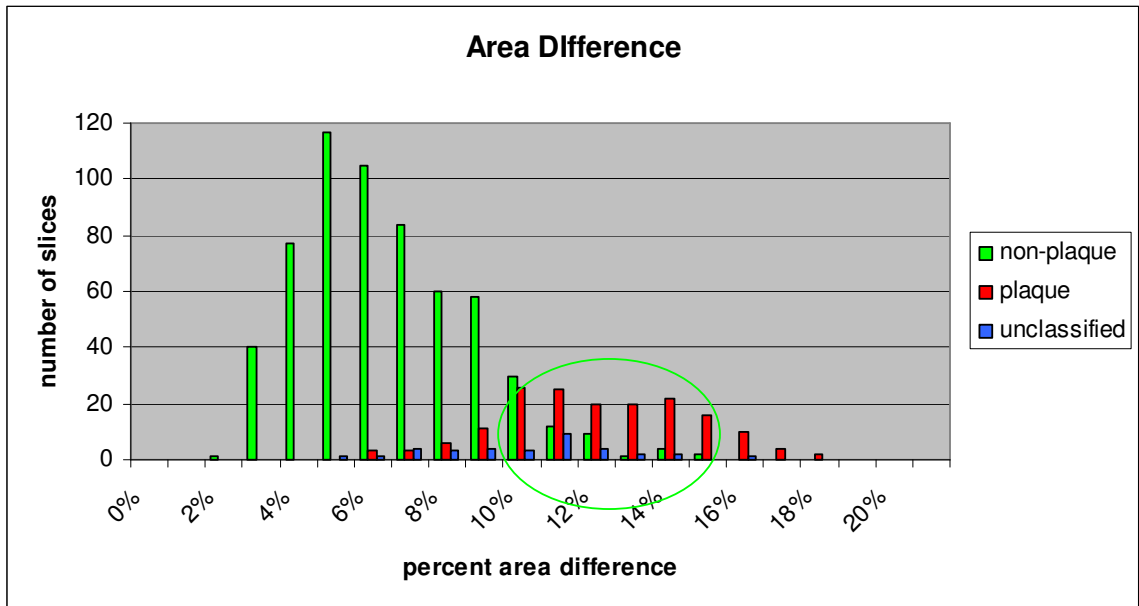
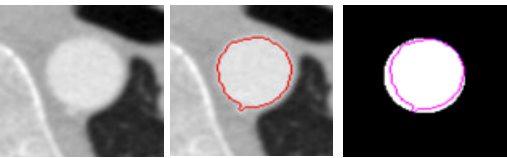
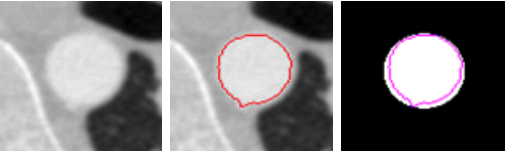
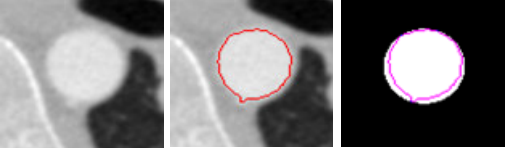
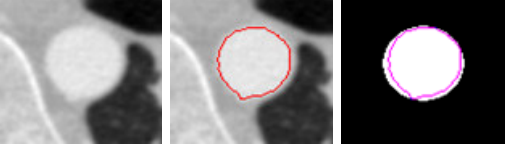
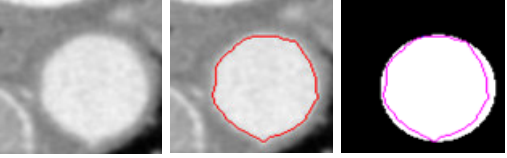
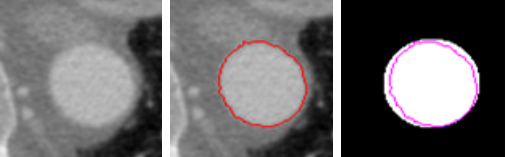
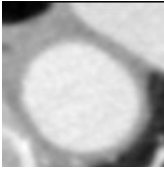
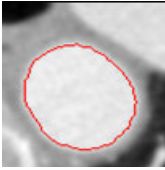

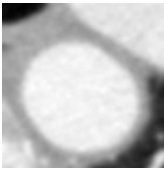
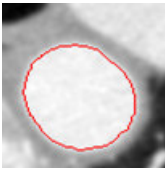

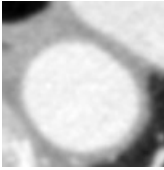
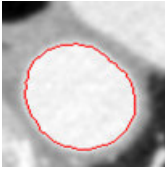

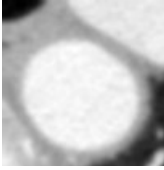
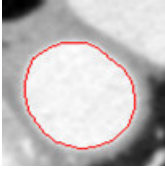

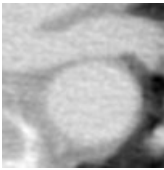
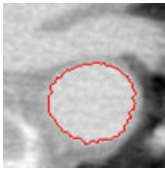

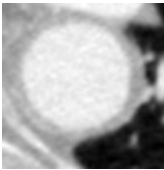
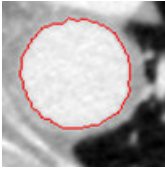



Figure 53: The green oval highlights the area of false positive slices.

slice identification	circularity	area difference	centroid displacement	fractal dimension
FC_P75_00010207.tif	0.9556	14.5%	7.4%	0.980
				
FC_P75_00010205.tif	0.9688	14.4%	5.0%	0.984
				
FC_P75_00010206.tif	0.9656	14.0%	6.2%	0.985
				
FC_P75_00010204.tif	0.9862	13.3%	4.8%	0.983
				
BE_P75_00010112.tif	0.9847	13.1%	4.5%	0.915
				
A4_P75_00010006.tif	0.9563	13.0%	3.6%	0.946
				

(Continued on next page)

slice identification	circularity	area difference	centroid displacement	fractal dimension
BE_P75_00010207.tif	0.9827	12.6%	1.8%	0.894
				
BE_P75_00010209.tif	0.9884	11.9%	1.7%	0.941
				
BE_P75_00010208.tif	0.9876	11.8%	3.0%	0.931
				
BE_P75_00010210.tif	1.0042	11.7%	3.8%	0.937
				
BE_P75_00010113.tif	0.9918	11.6%	5.2%	0.924
				
FC_P75_00010116.tif	0.9466	11.5%	3.8%	0.882
				

(Continued on next page)

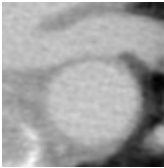
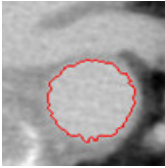

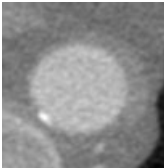
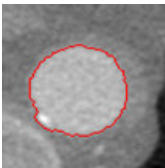

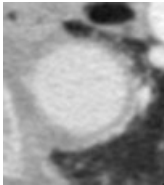
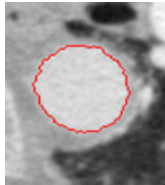

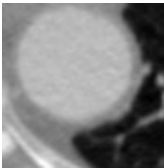
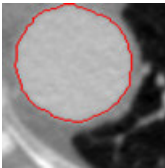

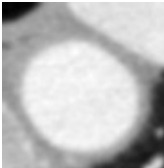
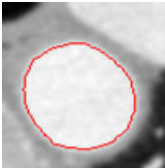

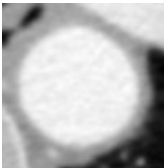
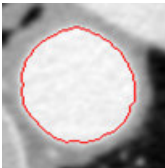

slice identification	circularity	area difference	centroid displacement	fractal dimension
A1 P75 00010018.tif	0.9678	11.5%	2.3%	0.937
				
A1 P75 00010087.tif	0.9073	11.3%	5.2%	0.942
				
BE P75 00010000.tif	0.9853	11.2%	4.2%	0.913
				
A1 P75 00010191.tif	0.9754	11.0%	0.4%	0.956
				
BE P75 00010212.tif	0.9894	10.9%	5.6%	0.930
				
BE P75 00010228.tif	0.9910	10.9%	2.6%	0.877
				

Figure 54: Image slices classified by physicians as having no visual indications of plaque that would not be correctly classified by area difference descriptor.

7.2 Combining the Descriptors

In the previous section, images which were misclassified by the area difference descriptor were presented. For many of these images, an alternate descriptor would have yielded the correct classification. Table 7 summarizes the results of fitting a logistic regression model [42] with each descriptor as the independent (predictor) variable and the reference classification (plaque = 1, non-plaque = 0) as the response variable.

From the output, p-values of less than 0.05 indicate that there is evidence of a relationship between each individual predictor and the response variable. The measurement of the concordant pairs is comparable to the estimated areas under the ROC curves. The measurement of the Goodman-Kruskal Gamma also indicates that the area difference descriptor has the best individual predictive ability.

Table 7: Individual Logistic Regression Results

Descriptor	p-value	Concordant Pairs %	Discordant Pairs %	Goodman Kruskal γ
Circularity	0.00	93.4%	6.5%	0.87
Centroid Displacement	0.00	79.4%	20.2%	0.59
Area Difference	0.00	94.6%	5.3%	0.89
Fractal Dimension	0.00	67.1%	32.3%	0.35

Since the logistic regression statistics indicated that each of the descriptors had merit in predicting the response variable, the first step in fitting the multiple logistic regression model included all four descriptors. The results are summarized in Table 8.

Table 8: Multiple Logistic Regression Result

Descriptor	Coefficient	p-value	Concordant Pairs %	Discordant Pairs %	Goodman Kruskal γ
Constant	17.4	0.008	97.2%	2.8%	0.94
Circularity	-34.4	0.000			
Centroid Displacement	15.7	0.103			
Area Difference	70.6	0.000			
Fractal Dimension	7.8	0.098			

In this case, the p-values for the circularity and the area difference descriptors indicate that there is evidence of a relationship between these predictors and the response variable.

Since the p-values for the centroid displacement and the fractal dimension are above 0.05, a reduced model should be considered. These models are summarized in Table 9. Both three-variable models indicate that circularity and area difference are the only two descriptors that are significant in this combined model. The p-values for centroid displacement and fractal dimension indicate that there is not sufficient evidence of a relationship between these predictors and the response variable. The concordant pairs and the Goodman-Kruskal gamma indicate that the simpler two-variable model has equal predictive ability. The percentage of concordant pairs indicates that the two-variable model is the best predictor of the response variable in this study.

Table 9: Reduced Multiple Logistic Regression Models

Descriptor	Coefficient	p-value	Concordant Pairs %	Discordant Pairs %	Goodman Kruskal γ
Three predictors			97.1%	2.9%	0.94
Constant	25.9	0.000			
Circularity	-35.6	0.000			
Area Difference	70.6	0.000			
Centroid Displacement	13.8	0.157			
Three predictors			97.1%	2.8%	0.94
Constant	18.1	0.000			
Circularity	-33.9	0.000			
Area Difference	75	0.000			
Fractal Dimension	6.8	0.149			
Two predictors			97.1%	2.9%	0.94
Constant	25.6	0.000			
Area Difference	74.7	0.000			

8. FUTURE WORK

The images for this thesis were obtained from a limited number of cardiac CT studies and their geometric features were exploited to produce a binary classification of those slices exhibiting evidence of plaque as determined by medical experts. Validating this work by actual plaque measurements through technologies such as intravascular ultrasound (IVUS) could provide a more accurate, continuous scale of plaque involvement to evaluate the potential of each image descriptor. It could also be instructive to evaluate the effect of additional information such as patient age or sex on descriptor performance.

While this study focused on the features of the lumen border as a two-dimensional object, further information about the characteristics of plaque deposits might be obtained by developing descriptors that incorporate volume information by considering the neighboring slice geometry as outlined in the studies of Kurkure, Avila-Montes, and Kakadiaris [19] and Renard and Yang [20]. For example, a change in a descriptor value along the length of the aorta could also be an indication of an area of interest.

The evaluation of the time series descriptors was limited to a small amount of available data. The potential in estimating elastic properties from the image sequences merits further study. Elasticity is also an area where descriptors might be greatly influenced by the age of the patient in addition to any plaque burden that is present.

Finally, while this project focused on contrast-enhanced CT images, the techniques developed in this analysis may be applicable to MRI images of the aorta. Identifying plaque in MRI slices would be a significant improvement since MRI images are acquired without the use of ionizing radiation.

9. SUMMARY

This thesis compared morphological features from CT cross-sectional images of the aorta. Using an estimated outline of the lumen border, several static image descriptors were calculated and compared. The border was also used as a basis to compare the elastic properties of the aorta as the border outline varied in time during the cardiac cycle. The project compared how well these descriptors are able to identify slices exhibiting evidence of plaque as determined by medical experts.

All of the descriptors exhibited some evidence of predictive ability, but the strongest models were based on the area difference and the circularity. Each of these descriptors showed individual strength with maximum accuracy levels near ninety percent and predictive probabilities estimated by the areas under the ROC curves in the range classified as very good. Combining the strengths of these two predictors using a multiple logistic regression provided the strongest model.

BIBLIOGRAPHY

- [1] Hsiang-Ching Kung, Ph.D.; Donna L. Hoyert, Ph.D.; Jiaquan Xu, M.D.; and Sherry L. Murphy, B.S.; “Division of Vital Statistics, Deaths: Final Data for 2005”, U.S. Department of Health and Human Services, National Center for Health Statistics, Centers for Disease Control, National Vital Statistics System, Volume 56, Number 10, April 24, 2008.
- [2] Gil Kimel, MD, MSc; Gordon Andrews, MD; Bruce Forster, MD; Dean Malpas, “Multi-detector Computed Tomography of the Coronary Arteries—Pictorial Essay”
- [3] Ariel Cohen, “Atherosclerosis of the Thoracic Aorta: Further Characterization for Higher Risk of Vascular Events”, *J. Am. Coll. Cardiol.* 2008; 52:862-864
doi:10.1016/j.jacc.2008.04.063 <http://content.onlinejacc.org/cgi/content/full/52/10/862>, accessed September 2008.
- [4] Gerard J. Tortora and Bryan Derrickson, *Principles of Anatomy and Physiology*, John Wiley & Sons, Inc., 2006.
- [5] Tongfu Yu, MDa; Xiaomei Zhu, MDa; Lijun Tang, MDa; Dehang Wang, MDa; Nael Saad, MB, BCh; “Review of CT Angiography of Aorta”, *Radiologic Clinics of North America*.
- [6] J. Heuser, “File:Aorta scheme.jpg”,
http://commons.wikimedia.org/wiki/File:Aorta_scheme.jpg, accessed July 2009.
- [7] Stijn A.I. Ghesquiere, “File:Anatomy artery.png”,
http://commons.wikimedia.org/wiki/File:Anatomy_artery.png#file, accessed July 2009.
- [8] “Atherosclerosis”, American Heart Association, <http://www.american.heart.org>, accessed July 2009

- [9] “What is Coronary Artery Disease”, U.S. Department of Health and Human Services - National Institutes of Health,
http://www.nhlbi.nih.gov/health/dci/Diseases/Cad/CAD_WhatIs.html, accessed July 2009.
- [10] Itzhak Kronzon, MD; Paul A. Tunick, MD; “Aortic Atherosclerotic Disease and Stroke”, American Heart Association, Inc., *Circulation*. 2006; 114:63-75
<http://circ.ahajournals.org/cgi/content/full/114/1/63>, accessed October 2008.
- [11] Marco R. Di Tullio, Shunichi Homma, Zhezhen Jin, and Ralph L. Sacco, “Aortic Atherosclerosis, Hypercoagulability, and Stroke: The APRIS (Aortic Plaque and Risk of Ischemic Stroke) Study”, *J. Am. Coll. Cardiol.* 2008; 52: 855-861
<http://content.onlinejacc.org/cgi/content/full/52/10/855>, accessed September 2008.
- [12] Catherine L. Higgins, Seth A. Marvel, Joel D. Morrisett, “Quantification of Calcification in Atherosclerotic Lesions”, *Arteriosclerosis, Thrombosis, and Vascular Biology*. 2005; 25:1567, American Heart Association, Inc.
<http://atvb.ahajournals.org/cgi/content/full/25/8/1567>, accessed January 2009.
- [13] Mayo Clinic Staff, “CT Scan Definition” <http://www.mayoclinic.com/health/ct-scan/MY00309>, accessed July 2009
- [14] “OsiriX Imaging Software - About OsiriX”,
<http://www.osirix-viewer.com/AboutOsiriX.html>, accessed October 2008.
- [15] “File:Cardiac Cycle Left Ventricle.PNG”,
http://upload.wikimedia.org/wikipedia/commons/5/5b/Cardiac_Cycle_Left_Ventricle.PNG, accessed July 2009.

[16] “Musculoskeletal Imaging Hounsfield Unit” GE Healthcare, General Electric Company,
http://www.medcyclopaedia.com/library/topics/volume_iii1/hounsfield_unit.aspx,
accessed April 2009.

[17] Stephen Schroeder, MD; Andreas F. Kopp, MD; Andreas Baumbach, MD; Christoph Meisner, MA; Axel Kuettner, MD; Christian Georg, MD; Bernd Ohnesorge, PhD; Christian Herdeg; Claus D. Claussen, MD; and Karl R. Karsch, MD, FESC, FACC, FRCF; “Noninvasive detection and evaluation of atherosclerotic coronary plaques with multi-slice computed tomography”, *J Am Coll Cardiol*, 2001; 37:1430-1435,
<http://content.onlinejacc.org/cgi/content/abstract/37/5/1430>, accessed October 2008.

[18] Kiran R. Nandalur, Erol Baskurt, Klaus D. Hagspiel, C. Douglas Phillips, Christopher M. Kramer, “Calcified Carotid Atherosclerotic Plaque is Associated Less with Ischemic Symptoms Than Is Non-calcified Plaque on MDCT”, *American Roentgen Ray Society, AJR*:184, January 2005.

[19] U. Kurkure, O.C. Avila-Montes, I.A. Kakadiaris, “Automated segmentation of thoracic aorta in non-contrast CT images”, 5th IEEE International Symposium on Biomedical Imaging: From Nano to Macro, May 2008, Paris, Page(s):29 – 32.

[20] F. Renard and Y. Yang, “Coronary Artery Extraction and Analysis for Detection of Soft Plaques in MDCT Images”, 2008 5th IEEE International Symposium on Biomedical Imaging: From Nano to Macro, Paris, France, May 14-17, 2008 <http://www-video.eecs.berkeley.edu/Proceedings/ICIP2008/pdfs/0002248.pdf>, accessed January 2009.

[21] T.M. Nguyen and R.M. Rangayyan, “Shape Analysis of Breast Masses in Mammograms via the Fractal Dimension”, 27th Annual International Conference of the Engineering in Medicine and Biology Society 2005, Shanghai, January 2006, Page(s):3210 – 3213.

- [22] C. Stefanadis, J. Dernellis, E. Tsiamis, C. Stratos, L. Diamantopoulos, A. Michaelides and P. Toutouzas, “Aortic stiffness as a risk factor for recurrent acute coronary events in patients with ischemic heart disease”, *European Heart Journal* (2000) 21, 390–396.
- [23] V. Galante¹, C. Corsi, F. Veronesi¹, V. Russo, R. Fattori, and C. Lamberti, “Dynamic Characterization of Aorta Morphology and Function in Presence of an Aneurysm”, *Computers in Cardiology* 2007;34:765–768, <http://www.cinc.org/Proceedings/2007/pdf/0765.pdf>, accessed October 2008.
- [24] “NLM Insight Segmentation and Registration Toolkit (ITK)”, <http://www.itk.org/index.htm>, accessed October 2008.
- [25] “Enthought Scientific Computing Solutions - Products”, <http://www.enthought.com/products/epd.php>, accessed October 2008.
- [26] J. Wolfer, S.H. Lee, J. Sandelski, R. Summerscales, J.S. Soble, and J. Robergé, “Endocardial Border Detection in Contrast Enhanced Echocardiographic Cine-loops using a Pulse Coupled Neural Network”, *IEEE Computers in Cardiology*, September, 1999.
- [27] Charles Guse, Susan L. Gordon, A. Blake Robertson, and James Wolfer, “Exploring the Pulse Coupled Neural Network for Mammogram Preprocessing: a Preliminary Assessment”, *Proceedings of the Safety, Health, and Environment World Congress*, July, 2008 p21-25.
- [28] Adobe Systems “TIFF”, <http://partners.adobe.com/public/developer/tiff/index.html>, accessed June 2009.
- [29] Thomas Lindblad and Jason M. Kinser, *Image Processing using Pulse-Coupled Neural Networks*, Springer Verlag, 1998.

- [30] T. M. Nazmy, "Evaluation of the PCNN Standard Model for Image Processing Purposes", *IJICIS*, Volume 4, No. 2, July 2004.
- [31] John L. Johnson and Mary Lou Padgett, "PCNN Models and Applications", *IEEE Transactions on Neural Networks*, Vol. 10, No. 3, May 1999.
- [32] Li Yi, Tong Qinye, and Fan Yingle, "Texture Image Segmentation Using Pulse Coupled Neural Networks", *Second IEEE Conference on Industrial Electronics and Applications*, 2007, p355-359.
- [33] Donald A Cournoyer, "Breast Cancer Detection Using Difference of Gaussians and Pulse Coupled Neural Networks", Thesis, Graduate School of Engineering of the Air Force Institute of Technology, December, 1997.
- [34] J. Wolfer, J.S. Soble, and J. Robergé, "Enhancing Left-Ventricular Short-Axis Echocardiographic Cineloops with a Pulse Coupled Neural Network", *Environmental and Health World Congress*, Santos, Brazil, July16 - 19, 2006, p4-8.
- [35] Reinhard Eckhorn, "Neural mechanisms of scene segmentation: recordings from the visual cortex suggest basic circuits for linking field models", *IEEE Transactions on Neural Networks*, Volume 10, Issue 3, May 1999, pp.464-479.
- [36] W. Burger and M. Burge, *Digital Image Processing*, Springer, New York, 2008, pp.175, 211, 223-224.
- [37] E.R. Davies, *Machine Vision*, Morgan Kaufmann, San Francisco, California, 2005, pp.214-217, 287.
- [38] Phillip J. Schneider and David H. Eberly, *Geometric Tools for Computer Graphics*, Morgan Kaufmann Publishers, San Francisco, California, 2003, pp.807-811.

- [39] Kelly H Zou, A. James O'Malley, and Laura Mauri, "Receiver Operating Characteristic Analysis for Evaluating Diagnostic Tests and Predictive Models", *Circulation*, 2007; 115:654-657, downloaded from circ.ahajournals.org May 2009.
- [40] Tom Fawcett, "An Introduction to ROC Analysis", *Pattern Recognition Letters* 27, June 2006; 861-874.
- [41] Thomas G. Tape, MD, "Interpreting Diagnostic Tests", University of Nebraska Medical Center, <http://gim.unmc.edu/dxtests/Default.htm>, accessed January 2009.
- [42] James A. Hanley and Barbara J. McNeil, "The Meaning and Use of the Area Under a Receiver Operating Characteristic (ROC) Curve", *Radiology*, Vol. 143, No. 1, 29-36, April 1982.
- [43] Steve Simon, "Children's Mercy Hospitals and Clinics", <http://www.childrensmercy.org/stats/ask/roc.asp>, accessed July 2009.
- [44] Mark H. Zweig and Gregory Campbell, "Receiver Operating Characteristic (ROC) Plots: A Fundamental Evaluation Tool in Clinical Medicine", *Clinical Chemistry*, Vol. 39, No. 4, 562-577 (1993).
- [45] Minitab 15, Minitab, Inc., 2009.
- [46] "How do I interpret odds ratios in logistic regression?", UCLA: Academic Technology Services, Statistical Computing Group, http://www.ats.ucla.edu/stat/mult_pkg/faq/general/odds_ratio.htm, accessed October 2009.
- [47] "Logistic Regression", <http://luna.cas.usf.edu/~mbrannic/files/regression/Logistic.html>, accessed October 2009.